

# Intense Electromagnetic Outbursts from Collapsing Hypermassive Neutron Stars

Luis Lehner<sup>1,2,3</sup>, Carlos Palenzuela<sup>4</sup>,

Steven L. Liebling<sup>5</sup>, Christopher Thompson<sup>4</sup>, Chad Hanna<sup>2</sup>

<sup>1</sup>*Department of Physics, University of Guelph, Guelph, Ontario N1G 2W1, Canada,*

<sup>2</sup>*Perimeter Institute for Theoretical Physics, Waterloo, Ontario N2L 2Y5, Canada,*

<sup>3</sup>*CIFAR, Cosmology & Gravity Program, Canada,*

<sup>4</sup>*Canadian Institute for Theoretical Astrophysics, Toronto, Ontario M5S 3H8, Canada,*

<sup>5</sup>*Department of Physics, Long Island University, New York 11548, USA*

We study the gravitational collapse of a magnetized neutron star using a novel numerical approach able to capture both the dynamics of the star and the behavior of the surrounding plasma. In this approach, a fully general relativistic magnetohydrodynamics implementation models the collapse of the star and provides appropriate boundary conditions to a force-free model which describes the stellar exterior. We validate this strategy by comparing with known results for the rotating monopole and aligned rotator solutions and then apply it to study both rotating and non-rotating stellar collapse scenarios, and contrast the behavior with what is obtained when employing the electrovacuum approximation outside the star. The non-rotating electrovacuum collapse is shown to agree qualitatively with a Newtonian model of the electromagnetic field outside a collapsing star. We illustrate and discuss a fundamental difference between the force-free and electrovacuum solutions, involving the appearance of large zones of electric-dominated field in the vacuum case. This provides a clear demonstration of how dissipative singularities appear generically in the non-linear time-evolution of force-free fluids. In both the rotating and non-rotating cases, our simulations indicate that the collapse induces a strong electromagnetic transient, which leaves behind an uncharged, unmagnetized Kerr black hole. In the case of sub-millisecond rotation, the magnetic field experiences strong winding and the transient carries much more energy. This result has important implications for models of gamma-ray bursts. Even when the neutron star is surrounded by an accretion torus (as in binary merger and collapsar scenarios), a magnetosphere may emerge through a dynamo process operating in a surface shear layer. When this rapidly rotating magnetar collapses to a black hole, the electromagnetic energy released can compete with the later output in a Blandford-Znajek jet. Much less electromagnetic energy is released by a massive magnetar that is (initially) gravitationally stable: its rotational energy is dissipated mainly by internal torques. A distinct plasmoid structure is seen in our non-rotating simulations, which will generate a radio transient with subluminal expansion, and greater synchrotron efficiency than is expected in shock models. Closely related phenomena appear to be at work in the giant flares of Galactic magnetars.

## I. INTRODUCTION

Understanding the gravitational collapse of a massive neutron star is of central importance for its connection to some of the most energetic astrophysical phenomena. Such an event may take place within a core-collapse supernova [1], or in the late stage of a binary neutron star merger [2, 3], and is widely believed to power some types of gamma-ray bursts. In recent years it has been realized that newly formed stellar mass black holes may be prodigious sources of electromagnetic energy, in addition to driving strong kinetic outflows [1, 4–6]. We are faced with the exciting possibility of probing the most extreme forms of gravitational collapse using coordinated measurements of electromagnetic transients and gravitational waves. Refining models that make observational predictions for joint gravitational and electromagnetic radiation is critical in order to establish efficient observation campaigns for both traditional astronomers and gravitational-wave astronomers. It is also a key step toward predicting the delay between peak electromagnetic and gravitational wave emission, the electromagnetic emission pattern (i.e. the beaming angle) and the electromagnetic and gravitational wave spectrum.

Our focus here is on the evolution of the neutron star's magnetic field during its collapse to a black hole. We employ fully self-consistent relativistic calculations that follow the dense stellar material as well as the strong electromagnetic and gravitational fields. A particularly intense electromagnetic transient is generated if the initial magnetic field is very strong ( $\sim 10^{15} - 10^{16}$  G), that is, if the star is a magnetar. Rapid rotation will enhance the energy of the transient, to a degree that can only be derived by a full time-evolution of the electromagnetic and gravitational fields. Rapid rotation also provides a context for generating strong magnetic fields: when the neutron star is accreting, the shear layer at its surface is a promising site for dynamo action. A distinct magnetosphere will emerge and hold off the accretion flow if even  $\sim 10^{-4} - 10^{-3}$  of the energy that is dissipated in the shear layer is converted to a poloidal magnetic field. Understanding the evolution of the magnetic field around an *isolated* star is therefore potentially of key relevance for the collapsar and binary merger scenarios of gamma-ray bursts.

Recent success in studying the behavior of plasmas around magnetized, spinning, stable neutron stars within flat spacetime has been presented in Refs. [7–9]. To study

the collapse problem, one needs general relativity – to account for the role of spacetime curvature; and general relativistic magnetohydrodynamics (GRMHD) – to determine the internal evolution of the star. The electromagnetic (EM) phenomena outside the star can be approached in a variety of ways: through a full GRMHD calculation, which generally is very expensive given the low matter density; or more approximately using vacuum EM and force-free equations. In this paper, we compare all three approaches (restricting to ideal MHD in the case of GRMHD).

Within general relativity, studies paying attention to neutron star collapse have been presented in the context of isolated stellar collapse (e.g. [10–14]) and binary neutron star mergers (e.g. [15–20]) with different degrees of realism. The role of electromagnetic fields are typically examined within general relativistic *ideal* MHD and studies have been presented for single [21–26] and binary star systems [17, 18, 27]. Such simulations have illustrated important details of the extreme dynamical behavior induced by the system which could trigger tremendously energetic phenomena.

Newtonian and general relativistic simulations have shed light on how a binary neutron star merger can amplify pulsar-strength magnetic fields by several orders of magnitude [18, 27–29]. The resulting hypermassive star is generically unstable to black hole formation, which opens up the tantalizing possibility that the increasing rotation rate and magnetic field strength would drive an intense electromagnetic outflow. To study such a scenario, our goal here is to combine the GRMHD approach with a suitable description of the magnetically-dominated region outside a collapsing star, by applying the force-free approximation. Our approach is related to that of Ref. [30], which matched a simplified, analytic, relativistic solution for the interior of a collapsing star (dust-ball) with a numerical solution of the coupled Einstein-Maxwell equations in its exterior. Boundary conditions at the star’s surface are provided by the analytic, ideal MHD solution.

We go beyond this simplified scenario in three significant ways. First, our stars are evolved through collapse consistently by evolving the ideal GRMHD equations, and we can therefore consider in principle any kind of compact star. In particular, we have studied both rigidly rotating and non-rotating stars, whereas only the non-rotating case was considered in [30]. Second, the magnetosphere is described within the force-free approximation, which, as argued in Ref. [31], is a much more realistic model that, for instance, has been instrumental in understanding pulsar spin down [8]. Third and last, our matching of the exterior solution with the interior one is dynamical. Thus the force-free solution can adapt to time-dependent fields sourced by the star.

Our approach thus allows us to examine many interesting scenarios and we apply it here to study the behavior of collapsing, magnetized, compact stars (either rotating or not), the behavior of surrounding plasma (as described

within the force-free approximation) and possible electromagnetic radiation induced by the system. We compare our results with recent estimates in Ref. [32] for the non-rotating case which predict that the collapse process is smooth and that the magnetic field remains anchored to the star as a black hole forms, leaving a final black hole with a split-monopole field configuration. Our work, which follows the dynamics of the system, indicates that in both cases the stars radiate significant electromagnetic energy in which reconnection plays a crucial role, and that this radiation ceases shortly after the formation of a black hole. With force-free, such a black hole loses its electromagnetic hair within a dynamical time scale.

We describe our hybrid approximation and the evolution equations in Sec. II, followed by a summary of the numerical techniques in Sec. III. Our choice of initial data is described in Sec. IV, and several tests of the hybrid approach are presented in Sec. V. The new results for collapsing, magnetized stars are explained in detail in Sec. VI, while the astrophysical consequences are described in Secs. VII and VIII. We conclude in Sec. IX with some final comments.

## II. APPROACH

In the presence of matter and electromagnetic fields, the Einstein equations must be suitably coupled to both the Maxwell and hydrodynamics equations. This coupling is achieved by considering the stress energy tensor

$$T_{ab} = T_{ab}^{\text{fluid}} + T_{ab}^{\text{em}}, \quad (1)$$

with contributions from matter and electromagnetic energy given respectively by

$$T_{ab}^{\text{fluid}} = [\rho_o (1 + \epsilon) + P] u_a u_b + P g_{ab}, \quad (2)$$

$$T_{ab}^{\text{em}} = F_a{}^c F_{bc} - \frac{1}{4} g_{ab} F^{cd} F_{cd}. \quad (3)$$

A perfect fluid with pressure  $P$ , energy density  $\rho_o$ , internal energy  $\epsilon$ , and four-velocity  $u^a$  describes the matter state, and the Faraday tensor  $F_{ab}$  describes the electromagnetic field. The fluid and electromagnetic components are directly coupled through Ohm’s law, which closes the system of equations by defining the electric current 4-vector  $J_a$  as a function of the other fields. A general relativistic expression can be obtained by considering a multifluid system of charged species [33], leading to a fully non-linear propagation equation for the spatial component of the current. However, it usually suffices to consider a simplified version accounting for an algebraic relation between the current and the fields [34]

$$J^a + (u_b J^b) u^a = \sigma^{ab} F_{bc} u^c, \quad (4)$$

where  $\sigma^{ab}$  is the conductivity of the fluid. The well-known scalar Ohm’s law is recovered for  $\sigma^{ab} = g^{ab} \sigma$ .

The equation of motion for the fluid and electromagnetic field are obtained from *the conservation laws*

$$\nabla_a T^{ab} = 0 ; \nabla_a (\rho_o u^a) = 0 ; \quad (5)$$

$$\nabla_a F^{ab} = J^b ; \nabla_a {}^*F^{ab} = 0 ; \quad (6)$$

which, together with the Einstein equations  $G_{ab} = 8\pi T_{ab}$ , complete the system of equations governing the dynamics.

Once the appropriate form of Ohm's law and the conductivity have been specified, using for instance the algebraic relation of Eq. (4), the resulting equations typically involve vastly different scales, rendering the implementation of these equations quite costly from a computational point of view [114]. Fortunately, for specific regimes certain useful approximations capture the *most relevant* physics while bypassing the most strenuous difficulties. For our current purposes, involving magnetized neutron stars, the following relevant approximations can be defined and employed in different regimes:

- The *ideal-MHD* equations are obtained by requiring that the current remains finite in the limit of infinite conductivity,  $\sigma \rightarrow \infty$ . This condition also implies the vanishing of the electric field measured by an observer co-moving with the fluid ( $F_{ab}u^b = 0$ ). This approximation is appropriate for the highly conducting matter expected in neutron stars. However, the numerical evolution of the ideal MHD equations typically fails in low density regions where the inertia of the electromagnetic field is a few orders of magnitude larger than that of the fluid unless sufficient resolution is available. Such resolution requirements increase as the ratio of the electromagnetic to the fluid's inertia (or magnetic to fluid's pressure) grows. Consequently, the approach becomes costlier in regions with decreasing physical relevance with respect to bulk matter motion. Such a situation arises in particular in "vacuum" regions due to the standard practice of maintaining a density floor (a so called *atmosphere*) in regions of low density to exploit advanced numerical techniques for relativistic hydrodynamics. The atmosphere's density is much smaller than that inside the star, so this approach does not affect the relevant matter physics. However outside the star, the fluid inertia (or pressure) is typically much smaller than that of the electromagnetic field in magnetized cases and one generally encounters a large number of numerical difficulties. Different numerical strategies are often introduced to avoid them but such measures can limit one's ability to extract appropriate physics in these regions.
- The *force-free* Maxwell equations are obtained by assuming the fluid's inertia is much smaller than that of the electromagnetic fields. As a result  $F_{ab}J^b = 0$  which in turn implies  $F_{ab}{}^*F^{ab} = 0$  ( $\rightarrow E \cdot B = 0$ ) [31, 35]. This assumption therefore

allows one to ignore the explicit time-evolution of the fluid as its dynamics are implicitly prescribed by the charge and current distribution. This approximation is well suited to the dynamics of the low density, magnetically dominated plasma surrounding a compact object, but it cannot account for the physics in dense regions.

- The *vacuum* Maxwell equations are trivially recovered assuming no coupling with matter ( $\sigma = 0$ ). This is a natural approximation in vacuum regions, far away from the compact objects of interest.

As mentioned, computational costs are presently major obstacles to employ the general equations. It is thus highly desirable to define a scheme able to model all the relevant regimes in highly dynamical systems simultaneously since none of these three approaches captures all the expected behavior. In particular we have in mind interacting binary neutron stars, black hole-neutron star binaries as well as the collapse of a magnetized star considered here. All three systems are believed to play an important role in understanding gamma ray bursts and other energetic events driven by compact stellar-mass objects.

In what follows, we describe and apply a *hybrid* approach which, while approximate, can account for the dynamical interaction of both gravitating and electromagnetically driven fluids. Such an approach allows one to study the magnetosphere's behavior, in particular energetics and field topology providing important clues for understanding relevant systems. To do so, we take into account that the electromagnetic inertia of a region with high conductivity (i.e. inside the star) would be orders of magnitude larger than that of the plasma region. Thus, we can ignore the back-reaction of the electromagnetic field in the plasma region onto that inside the star (i.e., a "passive" magnetosphere). We exploit this observation to define our approach, which employs both the ideal and force-free approximations suitably matched around the stellar surface. The matching procedure is such that the star's electromagnetic field provides the boundary conditions for the surrounding region treated with the force-free approximation, but the behavior of the magnetospheric plasma on the high density stellar interior is ignored.

Notice that this approach, in a sense, can be regarded as a natural extension of that adopted for studying pulsar-spin down by magnetosphere interactions [7, 8] to general relativistic dynamical contexts. In these works, only the behavior of the magnetospheric plasma is studied and the star's influence is accounted for by boundary conditions. We here account for the possible stellar dynamics and consequent influence on the boundary conditions defined for the force-free approximation.

In practical terms, we regard our system as described by two sets of electromagnetic fields: (i) the ideal MHD fields  $\{E^i, B^i\}$  and (ii) the force-free fields  $\{\tilde{E}^i, \tilde{B}^i\}$ , governed by their respective equations. Both sets of fields

are defined with respect to observers orthogonal to the spacelike hypersurfaces employed to foliate the space-time. Thus identifying the appropriate fields for matching is direct. The ideal MHD equations are evolved over the entire computational domain, as is customary. The matching region is determined by fluid density being some value above the vacuum region (though alternatives based on other physical quantities are obviously possible). In particular, the force-free fields are evolved only in regions where  $\rho_o < \rho^{\text{match}}$ . Dynamic boundary conditions are applied to the force-free fields on the surface at which  $\rho_o = \rho^{\text{match}}$  using the ideal MHD fields

$$\tilde{E}_{bc}^i = -\epsilon_{jk}^i v^j B^k; \quad (7)$$

$$\tilde{B}_{bc}^i = B^i. \quad (8)$$

These conditions are applied in the spirit of penalty techniques [36] in which the equations are modified with driving terms at boundary points in order to enforce the desired boundary condition. In particular, we extend the penalty technique across a number of grid points to effect both the boundary conditions and to “turn-off” the evolution of the force-free fields within the higher density regions. Notice that this extension is not mathematically rigorous, but its usage will be justified by examining the solution in different test applications and comparing with the expected behavior. In practice we define a smooth kernel  $F(x^i, x_{\text{match}}^i)$  defined as

$$F(\rho_o, \rho^{\text{match}}) = \frac{2}{1 + e^{2K(\rho_o - \rho^{\text{match}})}} \quad (9)$$

where typically we adopt  $K \approx 0.001/\rho_{\text{atmos}}$  and  $\rho^{\text{match}} \approx 200 - 2000 \rho_{\text{atmos}}$ , being  $\rho_{\text{atmos}}$  the value for the density of the atmosphere. In the collapsing cases studied, this value is rescaled in time by the ratio of maximum density to the initial maximum density (see appendix). The values found in Eqs. (7-8) along with the kernel Eq. (9) make their appearance in the equations determining  $\{\tilde{E}^i, \tilde{B}^i\}$  (together with “constraint cleaning” fields  $\{\tilde{\Psi}, \tilde{\phi}\}$ , introduced to ensure constraints are well behaved through the evolution [37]) which are

$$\begin{aligned} \partial_t \tilde{E}^i &= F \left( \mathcal{L}_\beta \tilde{E}^i + \epsilon^{ijk} \nabla_j (\alpha \tilde{B}_k) - \alpha \gamma^{ij} \nabla_j \tilde{\Psi} \right. \\ &\quad \left. + \alpha \text{tr} K \tilde{E}^i - 4\pi \alpha J^i \right) + \lambda(1 - F)(E_{bc}^i - \tilde{E}^i) \end{aligned} \quad (10)$$

$$\begin{aligned} \partial_t \tilde{B}^i &= F \left( \mathcal{L}_\beta \tilde{B}^i - \epsilon^{ijk} \nabla_j (\alpha \tilde{E}_k) - \alpha \gamma^{ij} \nabla_j \tilde{\phi} \right. \\ &\quad \left. + \alpha \text{tr} K \tilde{B}^i \right) + \lambda(1 - F)(B_{bc}^i - \tilde{B}^i), \end{aligned} \quad (11)$$

$$\begin{aligned} \partial_t \tilde{\Psi} &= F \left( \mathcal{L}_\beta \tilde{\Psi} - \alpha \nabla_i \tilde{E}^i 4\pi \alpha q - \alpha \sigma_2 \tilde{\Psi} \right) \\ &\quad - \lambda(1 - F) \tilde{\Psi}, \end{aligned} \quad (12)$$

$$\begin{aligned} \partial_t \tilde{\phi} &= F \left( \mathcal{L}_\beta \tilde{\phi} - \alpha \nabla_i \tilde{B}^i - \alpha \sigma_2 \phi \right) \\ &\quad - \lambda(1 - F) \tilde{\phi}. \end{aligned} \quad (13)$$

The final term on the right-hand side of these equations is a penalty factor, which is introduced to impose interface conditions and ensure that a discrete energy norm

is bounded. Details of this “penalty technique” are presented in [36] and examples of applications in general relativity can be found in [38]. The above equations, together with the Einstein and GRMHD equations are implemented as described in [25, 39, 40] to which we refer the reader for further details.

### III. NUMERICAL TECHNIQUES

We adopt finite difference techniques on a regular Cartesian grid to solve the system. To ensure sufficient resolution in an efficient manner we employ adaptive mesh refinement (AMR) via the HAD computational infrastructure that provides distributed, Berger-Oliger style AMR [41, 42] with full sub-cycling in time, together with an improved treatment of artificial boundaries [43]. The refinement regions are determined using truncation error estimation provided by a shadow hierarchy [44] which adapts dynamically to ensure the estimated error is bounded within a pre-specified tolerance. The spatial discretization of the geometry and force-free fields is performed using a fourth order accurate scheme satisfying the summation by parts rule, and High Resolution Shock Capturing methods based on the HLLE flux formulae with PPM reconstruction are used to discretize the fluid variables [15, 45]. The time-evolution is performed through the method of lines using a third order accurate Runge-Kutta integration scheme, which helps to ensure stability of the numerical implementation [18]. We adopt a Courant parameter of  $\lambda = 0.2$  so that  $\Delta t_l = 0.2 \Delta x_l$  on each refinement level  $l$ . On each level, one therefore ensures that the Courant-Friedrichs-Levy (CFL) condition dictated by the principal part of the equations is satisfied.

To extract physical information, we monitor several quantities: (i) the matter variables and spacetime behavior, (ii) the electromagnetic field configuration and fluxes, and (iii) the electromagnetic Newman-Penrose (complex) radiative scalar ( $\Phi_2$ ). This scalar is computed by contracting the Maxwell tensor with a suitably defined null tetrad

$$\Phi_2 = F_{ab} n^a \bar{m}^b, \quad (14)$$

and it accounts for the energy carried off by outgoing waves to infinity. The luminosity of the electromagnetic waves is

$$\begin{aligned} L_{\text{em}} &= \frac{dE^{\text{em}}}{dt} = \int F_{\text{em}} d\Omega \\ &= \lim_{r \rightarrow \infty} \int r^2 |\Phi_2|^2 d\Omega. \end{aligned} \quad (15)$$

Additionally we monitor the ratio of particular components of the Maxwell tensor

$$\Omega_F = \frac{F_{tr}}{F_{r\phi}} = \frac{F_{t\theta}}{F_{\theta\phi}}, \quad (16)$$



which, in the stationary, axisymmetric case, can be interpreted as the rotation frequency of the electromagnetic field [35].

#### IV. INITIAL DATA

Initial data for the hybrid equations involve the intrinsic metric ( $g_{ij}$ ) and extrinsic curvature ( $K_{ij}$ ) on a given hypersurface, as well as the magnetized fluid configuration in terms of its primitive variables ( $\rho, \epsilon, v^i, B^i$ ). The initial data for the geometry and the fluid of rigidly rotating neutron stars are provided by the LORENE package *Magstar* [46], which adopts a polytropic equation of state  $P = K\rho^\Gamma$  with  $\Gamma = 2$  rescaled to  $K = 100$ . Because the fluid inertia of a neutron star is many orders of magnitude larger than its electromagnetic one, the magnetic field will have a negligible effect on both the geometry and the fluid structure, and so it can be specified freely. Unless noted otherwise, in our simulations we have chosen a dipolar structure for the initial magnetic field. The electric fields are set by assuming the ideal MHD condition Eq. (7), with zero fluid velocity in the exterior region. Additionally, we require initial data for the force-free fields  $\{\vec{E}^i, \vec{B}^i\}$ . Inside the star, they are defined to be exactly the same as their ideal MHD counterparts. Outside the star, the magnetic field is well defined by the dipolar solution, while the electric field is computed by assuming that the magnetosphere rotates rigidly with the star up to  $R_e = 2R_s$  ( $R_s$  is the stellar radius), and imposing again the ideal MHD condition for the electric field. This configuration provides consistent data for the problem; however such data will not necessarily conform to the physical situation considered and so an unphysical early transient will be generated.

#### V. TESTING THE APPROACH

We first establish that the adopted procedure is indeed able to capture correctly the dynamics of relevant systems. Since the ideal MHD approximation is self-consistently evolved throughout the computational domain, our tests must address the behavior of the force-free fields. To do so, we first examine the convergence of our implementation and then illustrate that the approach provides the expected behavior by comparing with certain recently studied cases.

##### A. Non-rotating, magnetized star with a dipole magnetic field

Adopting a stable and non-rotating stellar solution with mass  $M = 1.63M_\odot$  and equatorial radius  $R_{\text{eq}} = 8.62$  km, from which we remove all initial pressure, we examine convergence of the force-free fields as the star collapses. This scheme contains “standard” sources of

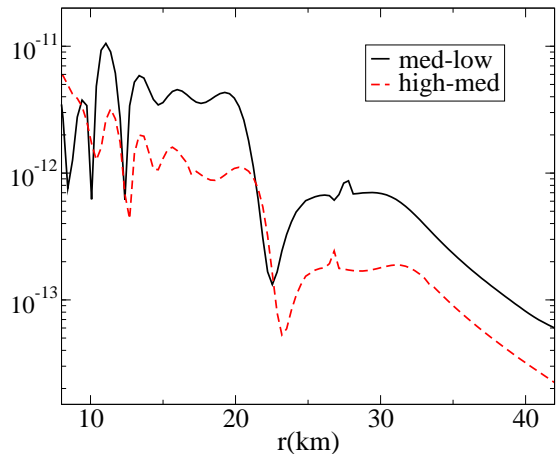


FIG. 1: *Non-rotating, collapsing solution.* Results from FMR solutions at three different resolutions for the same nonrotating collapsing star. Shown are the two differences between the resolutions. The difference in  $\vec{B}_z$  along  $y = 0$  in the equatorial plane at  $t = 0.06\text{ms}$  is first interpolated onto a uniform mesh for each solution. The difference between the *medium* and *high* resolutions is smaller than that between the *low* and *medium* resolutions, and this decrease as one increases the resolution indicates that the scheme is convergent. (Notice convergence in the central region is affected by initial data errors induced by depleting the pressure to induce the collapse.)

error, such as: (i) truncation error of our finite difference approximation of Maxwell’s equations, (ii) errors associated with our application of the force-free conditions, (iii) the various numerical errors (truncation and constraint violations) associated with our GRMHD implementation as well as (iv) errors associated with our dynamic boundary condition that matches the force-free fields to the corresponding MHD fields inside the star. A detailed analysis of these errors is delicate and involved; however we illustrate that the fields obtained by this approach converge to a unique solution with increasing grid resolution.

We therefore evolve the collapse of a non-rotating star at three different resolutions with fixed mesh refinement (FMR). We subtract a high resolution run (with coarse level grid of  $257^3$  points) and a medium resolution run (of dimension  $193^3$ ) and do similarly for the medium and low resolutions (of dimension  $129^3$ ). These two differences are plotted at  $t = 0.06\text{ms}$  (i.e., when the radius of the star starts to shrink) in Fig. 1 which shows that the difference decreases with increasing resolution, consistent with convergence.

##### B. Magnetic monopole

Next we consider a stationary force-free solution representing a rotating neutron star with a monopole magnetic

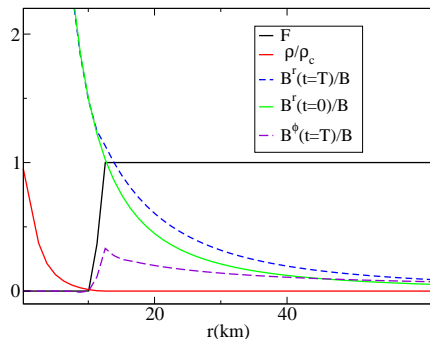


FIG. 2: *Monopole solution.* Specific components of the magnetic field displayed along the  $x = z = 0$  line at the initial and final times, together with the normalized density  $\rho/\rho_c$  and the  $F$  function. Notice that the radial component has a smooth transition across the surface of the star, while there appears a toroidal component in the magnetosphere.

field [47], and compare to our results. To minimize effects due to oscillations of the star (induced by perturbations to the star induced by the discretization), the geometry and MHD fields are kept to their initial values and are not evolved. The initial data correspond to a rigidly rotating neutron star near the mass shedding limit, with a mass  $M = 1.84M_\odot$  and an equatorial radius  $R_{\text{eq}} = 12$  km, rotating with a period of  $T = 0.886$  ms. The magnetic field is given by  $B^r = \alpha B_0 (R_s/r)^2$ , regularized conveniently near the origin. As described earlier, the initial electric field satisfies the ideal MHD condition in a rigidly co-rotating magnetosphere which extends initially up to  $R_e \sim 2R_s$ . The evolution is performed in a cubic domain of length  $L = 136$  km  $\approx 14 R_s$  with only two FMR grids and the star is placed at the origin. The maximum resolution is  $\Delta x = 0.72$  km, so that roughly 30 grid points cover the star. This resolution is sufficient for this test as both the geometry and matter variables are kept fixed and only the force-free equations are evolved until reaching a quasi-stationary configuration.

The behaviour of different fields across the surface of the star after the solution has settled are displayed in Fig. 2, which plots radial profiles of: the kernel function  $F$ , the density  $\rho_o$ , and the non-trivial components of the magnetic field. As illustrated in the figure, the radial magnetic field only changes outside the star, where there also appears a toroidal component indicating the rotation of the magnetic fields in the magnetosphere. Overall the electromagnetic fields are seen to relax rather quickly to a state approaching the expected one. Another measure of the obtained solution is given by the (normalized) rotational frequency of the magnetic field  $\Omega_F$  in Fig. 3. As time progresses, this value approaches 1 as expected in a radially smooth way.

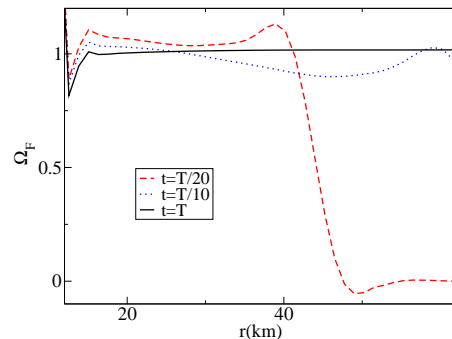


FIG. 3: *Monopole solution.* The rotation of the magnetic field lines (normalized with respect to its initial value) at different times inside and outside the domain, separated by the kernel function  $F$  (continuous line). As time progresses, the rotation frequency approaches the constant value expected for the monopole solution.

### C. Aligned rotator

A particularly challenging test of our approach is the aligned rotator solution (see [8]). The aligned rotator is a numerical solution of the force-free equations outside a rotating surface representing a star that demonstrates closed field lines within the light cylinder (LC). This problem has been studied by a number of authors [7, 8, 48–50] working in flat space with a computational domain consisting only of the stellar exterior. In these works the star’s influence is accounted for through suitable boundary conditions derived from the expected electromagnetic field at its surface. These efforts were specifically motivated to obtain the solution in the magnetosphere of isolated pulsars and, in particular, to understand a possible spin-down mechanism that works even when the star’s dipolar field is aligned with its angular momentum.

As already mentioned, our approach differs in that we solve for the stellar interior, we work within curved space and our computational grid does not conform to the star’s geometry [115]. Because of these differences and also because our initial data for the force-free fields is only nonzero in the immediate neighborhood of the star, achieving the expected late-stage stationary solution dynamically constitutes a demanding test. We note that the time and length scales required for such a test with respect to a realistic star are too computationally demanding if we are to capture the main physical aspects of the solution (i.e. field topology, location of the light-cylinder, development of a current sheet, etc). Instead of a realistic star, we adopt a rapidly rotating star so that the light cylinder is brought closer to the star –

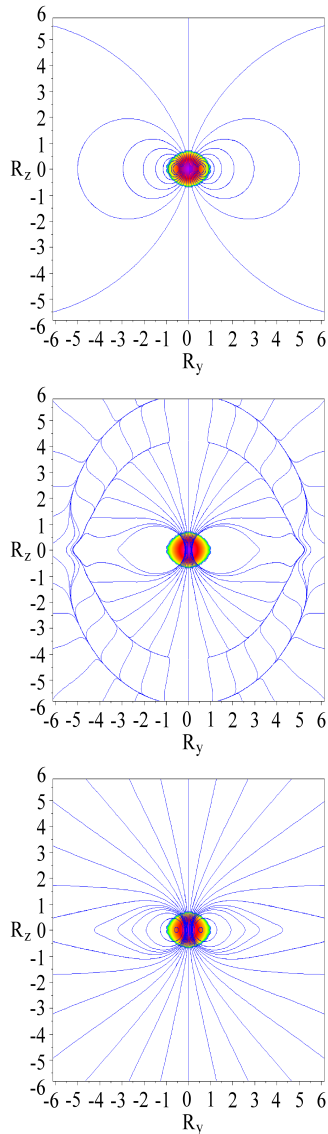


FIG. 4: *Aligned rotator.* The fluid density and the magnetic field lines on the  $x = 0$  plane at the four times  $t = (0, 1/3, 2/3)T$ . Even before a complete rotational period, the solution exhibits the known properties of the aligned rotator solution. The light cylinder is located roughly at the expected position  $R_{LC} \approx 3.6 R_s$  (large tick marks indicate one stellar radius  $R_s$ ). The intermediate plot illustrates the transient structure resulting as the LC forms and the initial data, which only extends to  $2R_s$ , relaxes to fill the computational domain. These plots do not show the entire computational domain.

where there is enough resolution to resolve it— and render the dynamical time scales shorter and easier to follow numerically. To achieve such rapid rotation, we resort to an unstable star but prevent the instability from disrupting the star by artificially freezing both fluid and geometry. Consequently we only evolve the force-free equations and compare the obtained configuration with the expected solution.

We adopt a rotating star with a mass  $M = 1.7M_\odot$ , equatorial/polar radius of  $R_{eq} = 8.5/6.0$  km and rotational period  $T = 0.64$  ms. The light cylinder for this star is located at  $R_{LC} = c/\Omega = 31$  km  $\approx 3.6 R_s$ . The electromagnetic field is initially set similar to that in the previous monopole test, but with a poloidal magnetic field given by a dipole outside the star. The evolution is performed in a cubic domain of  $L = 184$  km  $\approx 22 R_s$  with four FMR levels with resolutions  $\Delta x = (0.25, 0.5, 1.0, 2.0)$  km. The FMR hierarchy consists of centered cubes with side lengths  $L = (2.8, 5.6, 11.2, 22)R_s$ , so that there are roughly 70 points across the star in the equatorial plane.

We evolve this star until the solution settles to a quasi-stationary solution. Fig. 4 illustrates the magnetic field topology at three representative times. In the last frame, we show the configuration to which the field settles, illustrating features predicted by known solutions for the aligned rotator. In particular, one can observe a region of closed field lines bounded at the expected radius, denoting the light cylinder.

## VI. COLLAPSE OF A MAGNETIZED STAR

Having tested our hybrid approximation to EM field evolution, we now focus on the collapse of a magnetized star. The star may or may not be rotating, the rotating case being of greater astrophysical relevance. In particular, we are interested in studying how the magnetosphere responds, and the distribution of escaping electromagnetic radiation.

Here it is essential to capture both the dynamics of the collapsing star and the surrounding magnetoplasma, since the two are tightly coupled. It is worth recalling that the introduction of rotation introduces a fundamental difference in the radiative output of stationary (non-collapsing) stars as calculated in the electrovacuum and force-free limits: the spindown torque of an aligned rotator vanishes in electrovacuum but does not in the force-free case. Furthermore, this torque is strong and its magnitude varies only modestly with inclination angle [8].

Previous studies of the magnetosphere of a collapsing star are fairly limited. Some pioneering work in [51] focused on the electrovacuum behavior of a non-rotating star. While this study included the effects of strong gravity, by neglecting plasma or rotation it was not able to capture the winding of the magnetic field during the collapse. The analytic study by [32] estimated the EM output during the collapse by applying the formula for the spindown luminosity of an equilibrium rotator,  $L_{sd} \propto B_s^2 R_s^6 \Omega^4$ , where  $R_s$  is the stellar radius,  $B_s$  the surface magnetic field, and  $\Omega$  the spin frequency. However, when the collapse time is shorter than the rotation period (as must be the case if the star is to avoid a rotational hang-up), the outer magnetosphere near the light cylinder is not able to follow the change in the surface magnetic field, and this equilibrium formula does

not apply. Instead, twisting of the closed magnetic field lines is expected at a radius  $r_{\text{max}} \sim ct_{\text{col}}/3$  [116], where  $t_{\text{col}} \equiv R_s/|\dot{R}_s|$  is the collapse time. The corresponding toroidal magnetic field is  $B_\phi \sim (\Omega r_{\text{max}}/c)B(r_{\text{max}})$ , where  $B(r_{\text{max}}) \sim (3R_s/ct_{\text{col}})^3 B_s$  in a dipole geometry. The power injected into the magnetosphere is

$$L_{\text{sd}} \sim \frac{1}{6} B_s^2 R_s^2 c \left( \frac{\Omega R_s}{c} \right)^2 \left( \frac{3R_s}{ct_{\text{col}}} \right)^2 \quad (17)$$

which is larger than the equilibrium spindown power by a factor  $\sim (\Omega t_{\text{col}}/3)^{-2}$ .

To determine the dependence of  $L_{\text{sd}}$  on  $R_s$ , equation (17) must be combined with the conservation of magnetic flux,  $B_s R_s^2 = \text{constant}$ ; and the appropriate scaling between  $\Omega$  and  $R_s$  ( $\Omega \propto R_s^{-2}$  for self-similar collapse). The collapse does not, in general, follow a simple power-law relation between  $t_{\text{col}}$  and  $R_s$ , but in the special case of pressureless collapse from a large radius ( $t_{\text{col}} \propto R_s^{3/2}$ ) one obtains  $L_{\text{sd}} \propto R_s^{-4}$ . It should be re-emphasized that equation (17) represents energy stored in the magnetosphere, and so the maximum amount of energy that can only escape to infinity after the collapse is completed.

During the last, relativistic stages of the collapse, additional physical effects arise. Spacetime curvature has a mixed effect on magnetic field winding in the magnetosphere. On the one hand, the rotation frequency is reduced with respect to the Newtonian value; on the other hand, torsional Alfvén waves in the force-free magnetosphere slow down significantly as the horizon approaches the surface of the star.

The net result, as we show, is that the magnetic field becomes strongly wound up if the star is rotating close to breakup before the collapse, and develops  $a/M \gtrsim 0.5$  after the collapse. To clarify the influence of plasma and rotation, and to make useful comparisons, we have made a parallel set of runs in the electrovacuum approximation. These are obtained straightforwardly by setting  $J^i = 0$  and not enforcing the conditions  $\{E \cdot B = 0, |E| < |B|\}$  in Eqs. (10-13).

### A. Non-rotating stellar collapse

The collapse of a magnetized, but non-rotating, neutron star was studied in [30], where a magnetic field frozen into the stellar surface was matched to an exterior, vacuum solution of Maxwell's equations. This calculation followed the transition to a black hole, and the ringdown of the EM field threading the horizon.

In reality, the medium outside the star is an excellent electrical conductor. As is argued in [31, 35], a combination of large voltages and strong gravitational fields will trigger runaway pair creation near compact objects [31, 35]. In a strongly dynamic situation, the number of particles generated can be enhanced even further, e.g. by a Kolmogorov-like transfer of energy from large-scale waves to internal plasma heat [52]. The remnant of a binary merger or a rapidly rotating stellar core collapse is

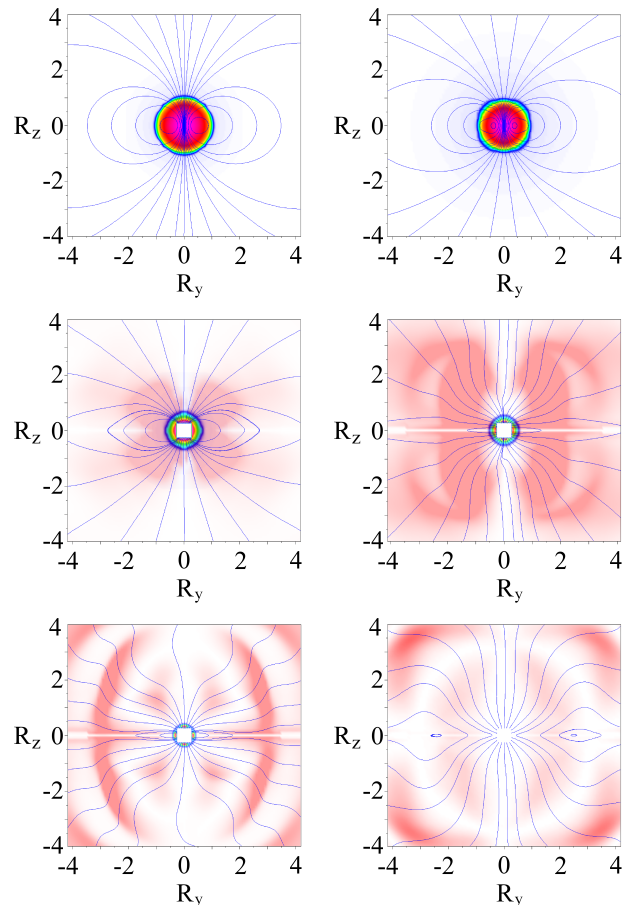


FIG. 5: *Non-rotating, unstable star (force-free)*. The fluid density (colors in the central region), the magnetic field lines (blue) and the EM radiation flux density (red) at times  $t = (-1, -0.2, 0.02, 0.05, 0.1, 0.2)$  ms (from left to right, top to bottom). Here  $t = 0$  denotes the time that the horizon appears. The magnetic field lines are dragged by the star during the collapse, producing Alfvén waves in the magnetosphere that carry a small fraction of the magnetospheric energy and stretch the magnetic field lines near the equatorial plane. Most of the EM energy falls into the black hole (the solid white, central rectangle denotes the excision region for the singularity).

also a strong neutrino source and, therefore, its magnetosphere will be filled with a much denser baryonic plasma compared with pulsar magnetospheres [53, 54]. But in most cases, the plasma around compact objects is magnetically dominated and its dynamics is nearly force free.

Therefore, we expect significant differences in the time evolution between the electrovacuum exterior assumed by [30] and a force-free magnetosphere. To anchor the external force-free (or electrovacuum) solution, we adopt a marginally unstable, non-rotating star with a mass  $M_s = 1.63M_\odot$  and a radius  $R_s = 8.62$  km. The numerical domain extends up to  $L = 16R_s$  and contains three centered FMR grids of sequentially half sizes (and



hence twice better resolved). The highest resolution grid has  $\Delta x = 0.18$  km.

The star collapses to a black hole in  $\sim 1$  ms [25]. We set  $t = 0$  at the onset of an apparent horizon and display the magnetic field and the density at various times in Fig. 5. This force-free solution has several salient features. There is an early transient in which the dipole magnetic field relaxes to a solution consistent with the physical configuration. Subsequently, as the star collapses, the magnetic field lines are gradually stretched along the equatorial plane. After 1.0 ms an apparent horizon appears in the interior of the star, which grows as it swallows all the remaining fluid in  $\sim 0.15$  ms. As the outer layers of the star are accreted by the black hole, the stretched magnetic field lines near the equatorial plane reconnect and form closed loops that carry away electromagnetic energy and magnetic flux (note the field loops in the last frame of Fig. 5).

The EM field evolution shows qualitative differences in the force-free and electrovacuum runs, especially after the black hole forms (Fig. 6). Starting from a common dipole structure at the beginning of the collapse, the magnetic field in the force-free case becomes radially stretched near the magnetic equator, and maintains a consistent sign. In the electrovacuum evolution, the stellar magnetic field disconnects more readily from the exterior. Changes in the connectivity of the magnetic field follow the appearance of zones where  $E^2 > B^2$ , as is demonstrated in Figs. 10 and 12.

For a more quantitative discussion, we consider in Fig. 7 the electric and magnetic fluxes, computed over a surface located at  $r = 1.5R_s$ , as a function of time. As expected, both the total (signed) fluxes remain small throughout the simulation, indicating that essentially no spurious magnetic/electric charges are created during the collapse. The unsigned magnetic flux decays exponentially in both the electrovacuum and force-free cases. Interestingly, the decay rate in the former case matches the  $l = 1, m = 0$  quasi-normal mode for electromagnetic perturbations of a Schwarzschild black hole with mass  $M = 1.63M_\odot$  [55].

The decay rate of the magnetic flux in the force-free run is roughly twice the electrovacuum result. One could translate the measured e-folding time  $t_E$  into an “effective reconnection speed,”  $V_{\text{rec}} \approx GMc^{-2}t_E^{-1}$  by observing that reconnection takes place within  $r \simeq (1 \rightarrow 2)r_H$  (with  $r_H$  the horizon radius). Our results indicate  $V_{\text{rec}} \simeq 0.14c$ .

This result may appear paradoxical at first sight, and deserves some comment. Electrovacuum magnetic fields effectively reconnect (by converting to electric-dominated fields) at the speed of light, as we discuss in more detail in Sec. VIA 4. Why then is the decay faster in the force-free case? The answer appears to reside in the self-inductance of the black hole. As magnetic field lines reconnect through the equator, they generate a strong toroidal EMF. In a vacuum, this EMF sources a magnetic flux of the opposing sign. When conducting matter

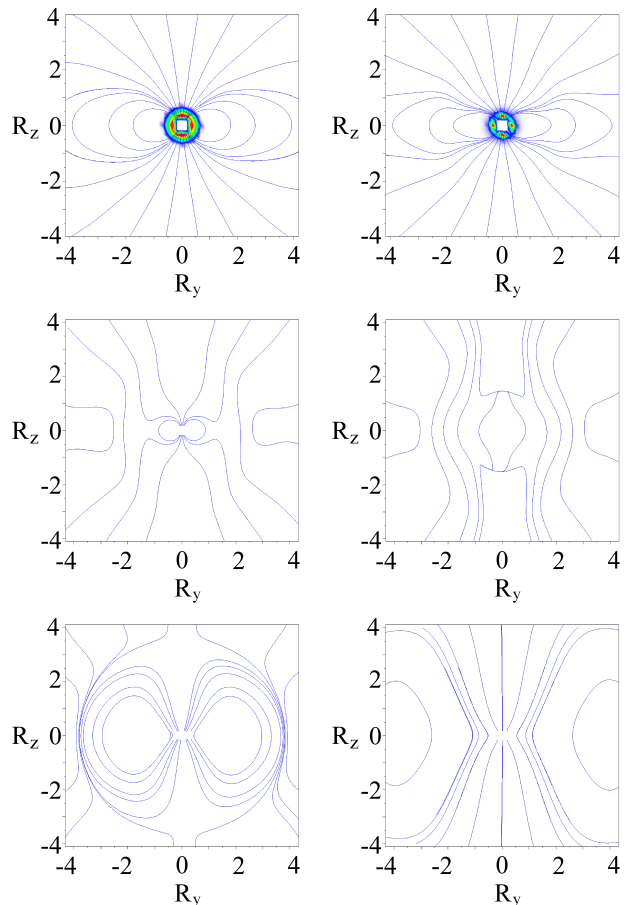


FIG. 6: *Non-rotating, unstable star (electrovacuum).* The fluid density (colors in the central region) and the magnetic field lines (blue) at  $t = (0.03, 0.06, 0.12, 0.125, 0.13, 0.15)$  ms. The magnetic field lines are dragged by the star during the collapse, stretching the magnetic field lines near the equatorial plane until that the fluid is swallowed by the black hole. Afterward, the EM dynamics is mostly described by the Quasi Normal Modes of the system.

is present, there is no oscillation in the sign of the flux threading the hole. Rather, reconnection is a monotonic process and, after the formation of an x-point, the magnetic field lines interior to the x-point fall through the horizon.

### 1. Electromagnetic Output

In order to estimate the efficiency with which EM energy is radiated to infinity, we have scaled the time-integrated luminosity to the peak electromagnetic energy contained in the magnetosphere. This peak energy is reached approximately at the formation of the apparent horizon. In the absence of rotation, it is  $C_{\text{peak}} \sim 2$  times the initial dipole energy, as determined by the conservation of magnetic flux. The measured radiated energy

is, in turn, a fraction  $\epsilon_{\text{rad}}$  of  $C_{\text{peak}} E_{\text{dipole},0}$ . Numerically,  $E_{\text{dipole},0} \approx (2\pi/3)(B_{\text{pole}}^2/8\pi)R_s^3 = (1/12)B_{\text{pole}}^2 R_s^3$ , and one finds  $E_{\text{dipole},0} = 1.4 \times 10^{47} B_{\text{pole},15}^2 \text{ erg}$  for a (initial) polar field  $B_{\text{pole}}$  and radius  $R_s \approx 12 \text{ km}$ . Hence

$$E_{\text{rad}} \approx 1.4 \times 10^{47} C_{\text{peak}} \epsilon_{\text{rad}} B_{\text{pole},15}^2 \text{ erg}. \quad (18)$$

The radiative efficiency is very small in the force-free case,  $\epsilon_{\text{rad}} = 0.008$ ; the rest of the peak energy is swallowed by the black hole. This is illustrated in Fig. 8, which shows how  $\epsilon_{\text{rad}}$  grows with time in both the force-free and electrovacuum runs. The radiated energy is  $E_{\text{rad}} \approx 10^{45} B_{\text{pole},15}^2 \text{ ergs}$ , from Eq. (18), expressed in terms of magnetar-strength magnetic fields. Most of this is radiated in a short interval  $\approx 1 \text{ ms}$  surrounding the collapse, with an average luminosity  $L \approx 10^{48} B_{\text{pole},15}^2 \text{ erg s}^{-1}$ .

The radiative efficiency measured at  $r = 1.5R_s$  is an order of magnitude higher in the electrovacuum case. This indicates that a larger proportion of the electromagnetic energy falls into the black hole in the force-free run, instead of escaping to infinity. An important check of this result is to measure the dissipation at current sheets in both the force-free and electrovacuum simulations. In both cases, we find that the integral of  $E \cdot J$  is a small fraction of the total EM energy in the magnetosphere. (The constraint  $E^2 < B^2$  is maintained in the force-free case by applying a small enhanced resistivity; hence the reduction in electric field energy appears as  $E \cdot J$  dissipation.)

An important feature of this radiation in both cases is its predominantly dipolar structure in energy flux (i.e.,  $L \propto \sin^2(\theta)$ ). In the force-free case, energy is radiated in a rather continuous manner and it propagates outwards with a velocity  $v = 0.89c$ , equivalent to a mild Lorentz factor of  $W = 2.2$ . For the electrovacuum case the energy is radiated mainly in two long bursts instead of the several, and with shorter periods, resulting in the force-free case.

## 2. Late Force-Free Evolution and Magnetic Reconnection

At later times, when the fluid has completely fallen into the black hole, the field lines that were dragged toward the horizon reconnect near the equatorial plane in a few sequential bursts, expelling most of the remaining magnetic flux. This behavior appears to be associated with the formation of x-type singularities in the magnetic field. Since the field is stretched radially and then reconnects near the horizon, the resulting electromagnetic pulse bunches up in the radial direction, which explains the structure seen in the last panel of Fig. 5.

X-point reconnection appears to happen easily in force-free plasmas; in ohmic plasmas it is associated with inhomogeneities in the electrical resistivity (e.g see [56]). In the absence of a detailed microphysical model for the resistivity, fine details such as these should be treated

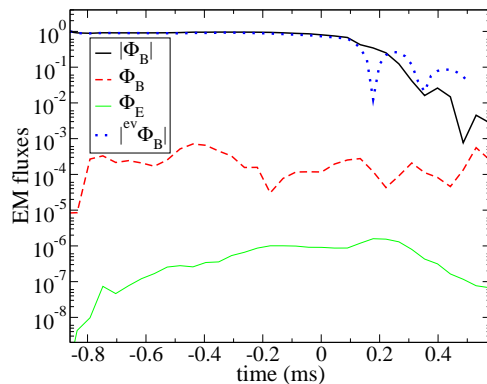


FIG. 7: *Non-rotating, unstable star*. The absolute value of the magnetic flux in the electrovacuum case as a function of time, and the electric and magnetic fluxes in the force-free case. These quantities are integrated over central spheres with radius  $r = 1.5R_s$  and normalized with respect to the initial integral of  $|\Phi_B(t=0)|$ . The total signed fluxes remain very small throughout the simulation, and the unsigned magnetic flux decreases as the black hole swallows all the matter which anchors the magnetic field.

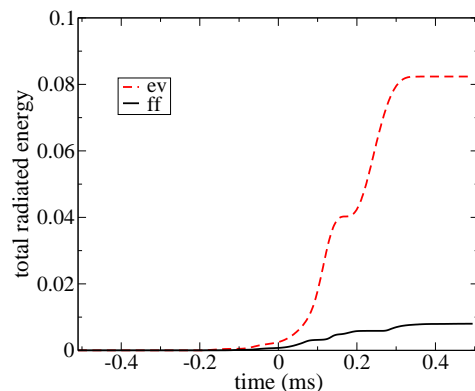


FIG. 8: *Non-rotating, unstable star*. Time integral of the electromagnetic luminosity, normalized with respect to the peak EM energy of the magnetosphere (i.e., around the formation of the black hole), in both the force-free and electrovacuum simulations. In the electrovacuum case, the net EM output is  $\sim 8\%$ , ten times larger than that radiated in the force-free case.

with caution, and the calculation should be viewed as illustrative.

## 3. Vacuum versus Force-Free EM Field Evolution in Axisymmetric, Non-Rotating Collapse

Some important features of the vacuum evolution of the electromagnetic field around a collapsing star can be understood by neglecting the effects of spacetime curvature, and by considering a simplified trajectory for the

surface of the star. If the collapse starts at a finite time, then an initially potential magnetic field evolves into a hybrid structure that consists of an inner potential magnetic field that matches the surface boundary condition as determined by the conservation of magnetic flux; and a transient electromagnetic wave that propagates into the original field structure.

Of especial interest is the appearance of zones within this wave structure that are dominated by the electric field. If the collapse continues for a long time (the final stellar radius  $R_s$  is small compared with the initial radius), then this zone where  $E^2 > B^2$  extends over a wide range of radius. Since a realistic magnetosphere may contain enough free charges to limit the growth of  $E \cdot B$ , this provides a nice example of how the nearly force-free evolution of an electromagnetic field can lead to strong dissipation.

In the absence of rotation, a spherically symmetric collapse implies a radial fluid velocity inside the star. As long as the stellar surface contracts with a speed  $-\dot{R}_s \ll c$ , the magnetic field near it is approximately potential. For a pure multipole of order  $\ell$ ,

$$\vec{B}(r) = B_s(t)R_s(t)\vec{\nabla} \left[ \frac{P_\ell(\cos \theta)}{(r/R_s)^{\ell+1}} \right] \quad (19)$$

(with  $B_s$  the magnetic field at the star's surface). A toroidal electric field  $E_\phi = -(\dot{R}_s/c)B_\theta$  is present at the surface of the star, assuming its interior to be perfectly conducting. The junction condition at the surface ensures the continuity of  $E_\phi$ . The surface magnetic field therefore increases in accordance with simple flux conservation,

$$\left. \frac{\partial B_s}{\partial t} + \dot{R}_s \frac{\partial B_s}{\partial r} \right|_{R_s} = -2 \frac{\dot{R}_s}{R_s} B_s. \quad (20)$$

At a fixed radius  $r$ , the magnetic field grows weaker: in the case of a simple dipole, the stellar magnetic moment scales as  $\mu(R_s) = B_s(R_s)R_s^3 = \mu_0(R_s/R_{s0})$ .

If the star were to reach infinite density at a finite time  $t_{\text{col}}$ , then a strong toroidal electric field would develop at  $r > c(t_{\text{col}} - t)$ . The inner potential zone would shrink along with the star as  $t$  approaches  $t_{\text{col}}$ .

The external electromagnetic field can then be obtained by rescaling the radius,  $r \rightarrow \xi \equiv r/R_s(t)$ , and transforming derivatives according to  $\partial_t X(r, t) \rightarrow [\partial_t + (\dot{R}_s/R_s)\partial_\xi]X(\xi, t)$ . It is simplest to solve for the vector potential  $A_\phi$ , from which the poloidal magnetic field and toroidal electric field are derived. The boundary condition at the surface of the star is

$$R_s(t)A_\phi[R_s(t), \theta] = \frac{B_s(t)R_s^2(t)}{\ell} \frac{dP_\ell}{d\theta} = \frac{R_{s0}A_{\phi 0}(\theta)}{\ell} \frac{dP_\ell}{d\theta}. \quad (21)$$

From Eq. (20),  $R_{s0}A_{\phi 0}(\theta)$  is constant. Substituting  $A_\phi(r, \theta) = R_{s0}A_{\phi 0}(\theta)g(\xi, t)$  into the wave equation

$$\partial_t^2(rA_\phi) = \partial_r^2(rA_\phi) - \frac{\ell(\ell+1)}{r^2}rA_\phi, \quad (22)$$

and adopting a collapse law  $R_s(t) \propto (t_{\text{col}} - t)^\alpha$  (here  $\alpha = 2/3$  for pressureless collapse from a large radius), we find

$$\begin{aligned} \partial_\tau^2 g + \frac{1}{\alpha} \partial_\tau g + 2\xi \partial_\tau \partial_\xi g &= \left[ \frac{c^2}{\dot{R}_s^2} - \xi^2 \right] \partial_\xi^2 g \\ &- \left( 1 + \frac{1}{\alpha} \right) \xi \partial_\xi g - \frac{c^2}{\dot{R}_s^2} \frac{\ell(\ell+1)}{\xi^2} g. \end{aligned} \quad (23)$$

Here  $\tau = \int \alpha dt / (t_{\text{col}} - t)$  is a dimensionless time coordinate; hence  $R_s(\tau) = R_{s0}e^{-\tau}$ . The electromagnetic field is constructed from the solution to Eq. (23) using

$$\begin{aligned} B_r(r, t) &= \frac{R_{s0}}{r^2} \frac{g(r/R_s, t)}{\sin \theta} \partial_\theta (\sin \theta A_{\phi 0}); \\ B_\theta(r, t) &= -\frac{R_{s0}A_{\phi 0}}{r^2} (\xi \partial_\xi g)_{\xi=r/R_s}; \\ E_\phi(r, t) &= -\frac{\dot{R}_s}{c} \frac{R_{s0}A_{\phi 0}}{rR_s} (\partial_\tau g + \xi \partial_\xi g)_{\xi=r/R_s}. \end{aligned} \quad (24)$$

One recovers the usual potential solution  $A_\phi(r, \theta) = A_{\phi 0}[R_s(t), \theta] (r/R_s)^{-(\ell+1)}$  where  $\xi \ll c/|\dot{R}_s|$ . A self-similar solution is also available in the case of collapse at a uniform speed,  $\alpha = 1$ , if the collapse starts at a very large initial radius. Then one can take  $\partial_\tau g = 0$  and the electromagnetic field is a function only of  $r/R_s$ . In this case, the magnetic field can retain a dipolar form out to large distances  $r \gg c(t_{\text{col}} - t)$  from the star. Restricting to  $\ell = 1$  gives

$$\begin{aligned} B_r(r, t) &= \frac{R_s}{R_{s0}} \frac{2\mu_0 \cos \theta}{r^3}; \\ B_\theta(r, t) &= \frac{R_s}{R_{s0}} \frac{\mu_0 \sin \theta}{r^3}; \\ E_\phi(r, t) &= \frac{r}{c(t_{\text{col}} - t)} B_\theta(r, t). \end{aligned} \quad (25)$$

Although the magnetic field is identical to that sourced by a stationary dipole of magnitude  $\mu(R_s) = \mu_0(R_s/R_{s0})$ , the electric field energy dominates outside a distance  $\sim (c/|\dot{R}_s|)R_s(t)$  from the star. The similarity solution is accurate out to the larger distance  $\sim (c/|\dot{R}_s|)R_{s0}$ , where  $R_{s0}$  is the stellar radius at the beginning of the collapse.

To understand how this inner solution for the electromagnetic field matches onto the initial potential magnetic field that was present prior to the collapse, or to consider cases other than constant  $\dot{R}_s$ , one must calculate the full time-dependent solution to (23). We have done this by evolving  $g(\xi, \tau)$ ,  $\partial_\tau g(\xi, \tau)$  and  $\partial_\xi g(\xi, \tau)$  using a centered discretization of Eq. (23) and employing a small Kreiss-Oliger dissipation value  $O(10^{-3})$  to damp high-frequency noise in each of these variables. The resulting electromagnetic field profile is plotted in Fig. 9, with distance normalized to the initial radius of the star. One observes in Fig. 10 the emergence of an extended zone with  $E^2 > B^2$ , as is expected from the similarity solution of Eq. (25). The magnetic field is relatively stronger in the polar regions, since  $A_\phi \propto \sin \theta \rightarrow 0$  at small  $\theta$ .

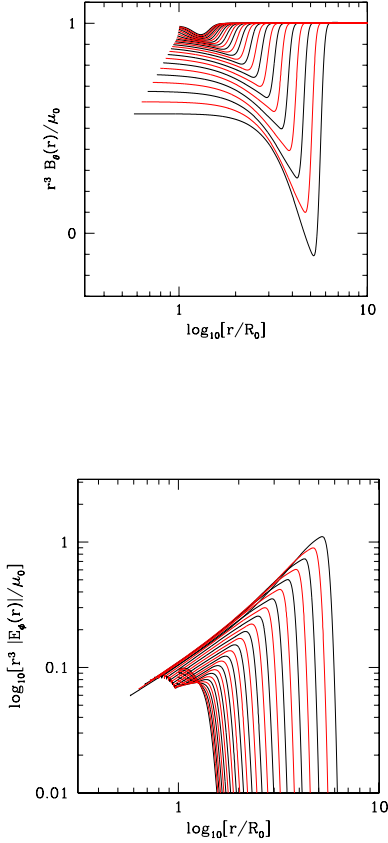


FIG. 9: *Evolving vacuum EM field around a star collapsing to half its initial size (uniform  $dR_s/dt$ ).* Top panel: the inner magnetic field tracks the instantaneous dipole of the collapsing star; at a fixed radius,  $B \propto \mu(R_s) \propto R_s/R_{s0}$ . Time progresses top to bottom. Bottom panel: The zone of rising  $E_\phi$  closely follows the similarity solution of Eq. (25). Time progresses left to right. (Two colours are employed for clarity.)

Eventually the amplitude of the outgoing wave disturbance becomes large enough that  $B_\theta$  changes sign. After this happens, the magnetic field remains dipolar inside the radius  $\sim (c/|\dot{R}_s|)R_{s0}$ , but disconnects from the external zone of undisturbed potential field. This transition is illustrated in Fig.11 using two snapshots corresponding to the two most extended field profiles in Fig. 9.

The first part of the collapse leads to a re-arrangement of the magnetic field outside the star, while electromagnetic energy flows inward: the Poynting flux,

$$S_r = -E_\phi B_\theta c \simeq -\frac{\dot{R}_s}{c} \frac{A_{\phi 0}^2(\theta) R_{s0}^2}{R_s(t)^4} \frac{(\partial_\xi g)^2}{\xi} \quad (26)$$

is negative inside  $r \sim (c/|\dot{R}_s|)R_{s0}$ . After the horizon forms and reaches the surface of the star, the compression of the magnetic field stops, and some of the trapped

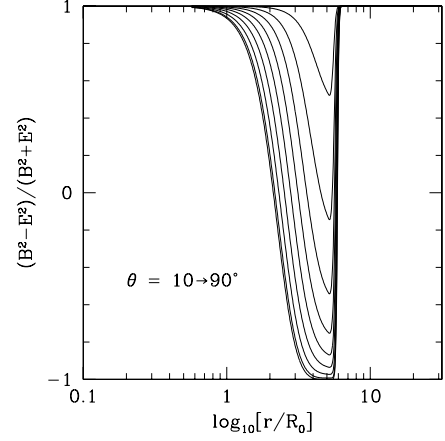


FIG. 10: *Relative strength of vacuum electric and magnetic fields around collapsing star (uniform  $dR_s/dt$ ).* Different lines illustrate the obtained behavior for different values of  $\theta$  (from  $10^\circ$ , top, to  $90^\circ$ , bottom). The zone where  $E^2 > B^2$  is more extended near the magnetic equator.

magnetic field can be radiated to infinity. The angular distribution of this radiated energy reflects the symmetry of the initial field. In the case of a dipole, the energy is carried away by closed magnetic loops and is mainly channeled through the magnetic equator.

We note that the appearance of zones with  $E^2 > B^2$  in the electrovacuum solution implies a fundamental difference with the alternative force-free solution. In this case,  $E \cdot B = 0$  throughout the collapse, so consistent force-free evolution is obtained only by removing energy from the electric field. From an MHD perspective, such a transition signals the appearance of nearly luminal plasma motions, where the inertia of even a small residue of entrained matter can become important.

This simple example shows that there can be profound differences in the macroscopic structure of the electromagnetic fields when even a small amount of conducting matter is present. In the complete absence of free charges, macroscopic zones where  $E^2 > B^2$  are the natural consequence of the time-evolution of an EM field that, initially, is purely magnetic.

#### 4. $E^2 > B^2$ in the Vector QNM of a Black Hole.

The quasi-normal mode (QNM) behavior observed shows two remarkable features: an oscillation in the sign of the magnetic flux threading each hemisphere, and the appearance of an equatorial zone with  $E^2 > B^2$ . These two features can be related to each other using a simple planar analogy.

Consider an initial magnetic field configuration  $\mathbf{B} = B_0 \hat{x}$  ( $-B_0 \hat{x}$ ) for  $y > 0$  ( $< 0$ ). This is familiar from studies of conducting fluids, where in the case of uniform



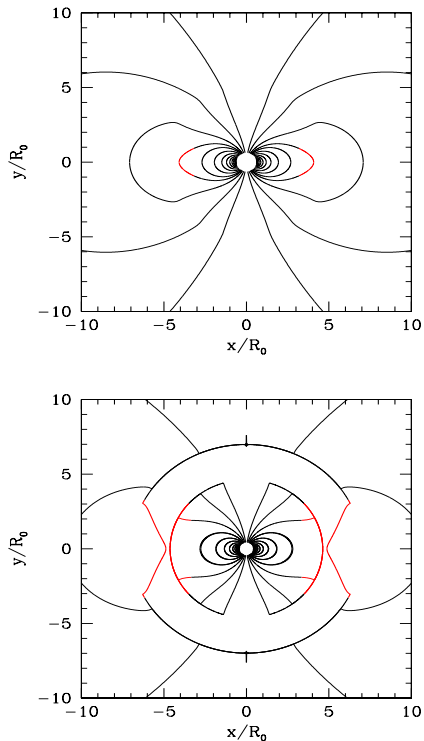


FIG. 11: *Connectivity of the magnetic field around a collapsing star (uniform  $dR_s/dt$ ).* The dipolar magnetic field that is anchored in the star disconnects from the surrounding, undisturbed, potential field when the amplitude of the output wave becomes large enough that  $B_\theta$  reverses sign. Note that  $E^2 > B^2$  (the red sections of the field lines) in the outer part of the inner zone with a dipolar magnetic field line profile. These two frames display the solution at the two latest times shown in Fig. 9 in which  $B_\theta$  becomes negative.

resistivity one finds a slow flow of matter to a thin current sheet at  $y = 0$ . The sheet thickness is limited by the flow of matter along the sheet to large  $|x|$  (Sweet-Parker reconnection). But now we are interested in the case where the conducting matter is absent, and the electromagnetic field evolves according to the vacuum wave equation. One finds, instead, a growing zone of pure electric field  $\mathbf{E} = -B_0 \hat{z}$  for  $|y| < ct$ , which maintains a uniform sign across the initial magnetic null surface. A pure magnetic field is converted to a pure electric field.

In the case of EM fields localized around a black hole, this conversion of magnetic to electric fields occurs at the magnetic equator, where the poloidal field lines merge together. The toroidal electric field that is created sources a poloidal magnetic flux through the horizon of the opposing sign to the pre-existing flux. In this way, a continuing interconversion of magnetic and electric fields can be maintained.

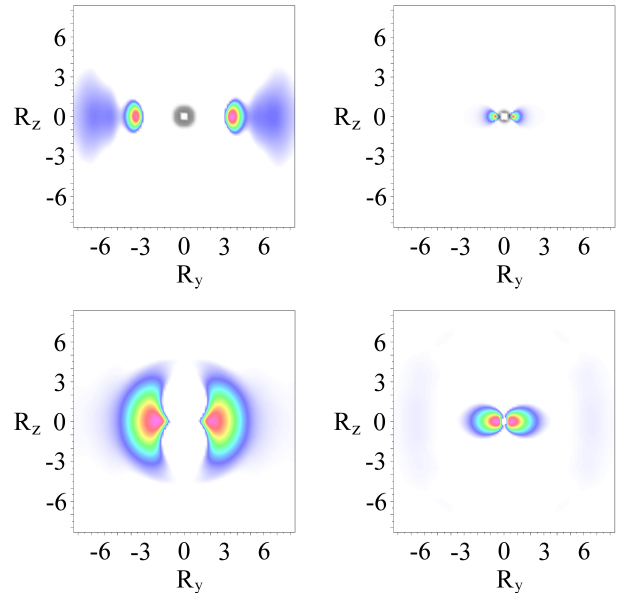


FIG. 12: *Non-rotating, unstable star (electrovacuum).* Electrically-dominated regions ( $E^2 > B^2$ ) are marked in color, at times  $t = (0.04, 0.13, 0.22, 0.31)$  ms. Here currents arise in the force-free case, and  $E^2 < B^2$  is maintained through gradual dissipation, resulting in a fundamental different with the electrovacuum evolution. As described by the simple Newtonian model, these regions form near the equatorial plane and close to the collapsing star. As time progresses, they propagate outward in bursts. The grey zone in the center represents the star.

## B. Rotating stellar collapse

The collapse of a rotating, magnetized star produces an interesting generalization of the relativistic wind problem for a stationary star (e.g [8, 31]). As in the case of spherical collapse, qualitatively new effects are introduced after the formation of a horizon. We have chosen an unstable, rotating model star with a mass  $M = 1.84M_\odot$  and equatorial radius  $R_s = 10.6$  km. The star rotates with a period  $T = 0.78$  ms, so that the light cylinder is initially located at  $R_{LC} = 37$  km  $\approx 3.5 R_s$ . The numerical domain and resolution are identical to those employed in the non-rotating case.

To remove unphysical transients we evolve the force-free equations for a couple of periods with both geometry and matter fixed, and afterwards all equations are evolved. This approach ensures the force-free fields relax to a configuration consistent with the physical scenario considered. The expected field configuration emerges during this startup phase, with a closed, corotating magnetosphere extending out to the light cylinder (LC). The Goldreich-Julian (G-J) current structure is present, with an outflow along the polar field lines balanced by a return flow through an equatorial current sheet.

The different stages of the collapse are represented in

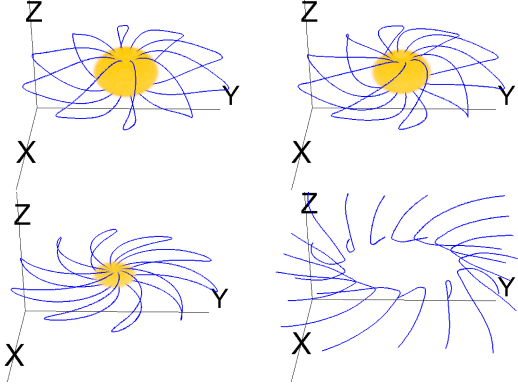


FIG. 13: *Rotating, unstable star (force-free)*. Magnetic field configuration (blue lines) and fluid density (marked in red) at times  $t = (-0.47, -0.17, -0.01, 0.12)$  ms. As the collapse proceeds the increasing spin rate of the star pulls the external magnetic field in the toroidal direction.

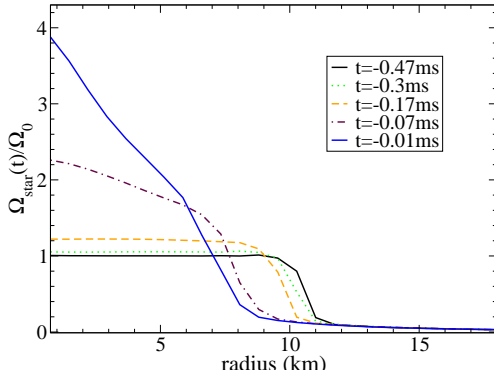


FIG. 14: *Rotating, unstable star (force-free)*. Star's angular rotational velocity, measured at the equator, during the collapse.

Fig. 13, while that the angular velocity of the star is displayed in Fig. 14. As the star contracts, and its rotational frequency increases, the instantaneous LC approaches the star[117]. Differential rotation develops in the magnetosphere, due to the lack of causal contact between the star and the LC, and the magnetic field is wound in the toroidal direction. Furthermore, the deepening of the gravitational potential forces significant changes in the magnetic field profile, by pulling the field lines more tightly toward the star.

The poloidal magnetic field strengthens due to flux freezing in the star, just as in the non-rotating case, but now most of the EM energy is in the toroidal component. Near the poles, the field lines twist around, generating a cone-like structure. In general, the magnetic field preserves a stretched dipolar topology for a longer time than in the non-rotating case, up to the point that all the fluid is swallowed by the black hole.

As the black hole forms inside the star, and the fluid

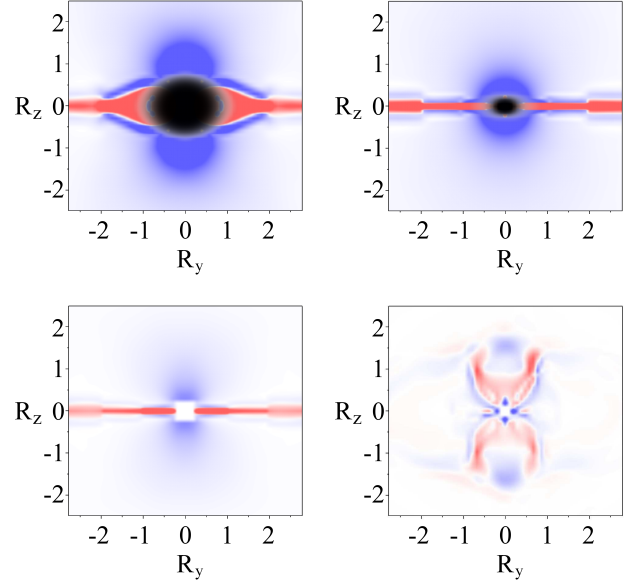


FIG. 15: *Rotating, unstable star (force-free)*. Charge density (blue: positive and red: negative) is plotted at  $t = (-0.17, -0.01, 0.12, 0.35)$  ms. The central fluid region marked in black disappears as the horizon emerges.

falls inward, many of the features in the EM field evolution are preserved from the non-rotating runs. Snapshots of the field profile, charge density and Poynting flux, taken at various times close to horizon formation, are displayed in Figs. 15 and 16. Just as in the non-rotating case, the topology of the magnetic field lines changes dramatically: the y-point structure in the magnetic field disappears from the equatorial regions, and a current sheet extends inward to the horizon. This current sheet is subject to spasmodic episodes of reconnection, the details of which may depend on the prescription for the electric resistivity and its variation with radius.

In less than a millisecond, the magnetic flux threading the horizon has almost completely vanished. This is qualitatively similar to the rapid evolution of a black hole interacting with a dipolar force-free configuration, as seen by [57]. In contrast with what is argued in [58], magnetic reconnection prevents the emergence of a relatively long-lived split-monopole configuration. In Sec. VIII A we discuss whether force-free or ideal MHD calculations more accurately describe the global structure of the current sheet, and the implications of the slower reconnection that is seen in the MHD calculation of [57].

The evolution of the magnetic flux during the collapse is displayed in Fig. 17, again computed on a surface located at  $r = 1.5R_s$ . The total (signed) flux is small through most of the simulation, and only at late times does it become comparable to the absolute value of the magnetic flux. In the electrovacuum case, the final decay is governed by the main quasi-normal modes of the rotating black hole. One observes faster decay in the force-free

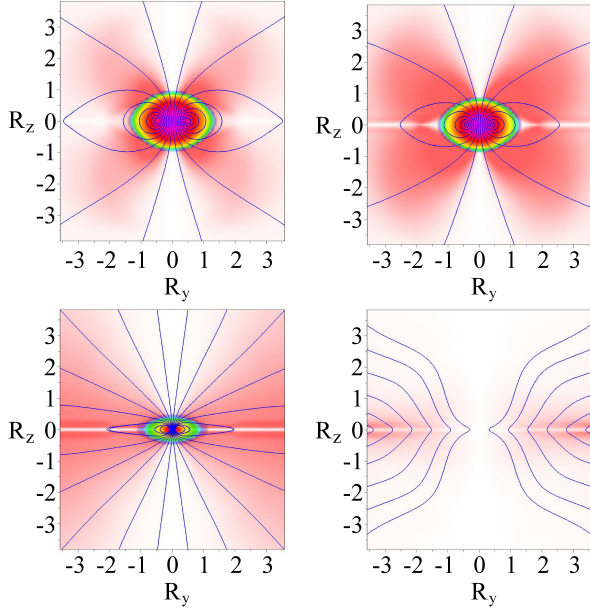


FIG. 16: *Rotating, unstable star (force-free)*. Radial Poynting flux in red at  $t = (-0.3, -0.17, -0.01, 0.12)$  ms. The central colored zones mark the stellar fluid. The evolution of the poloidal magnetic field (blue lines) in the equatorial regions is qualitatively similar to that observed in the non-rotating case.

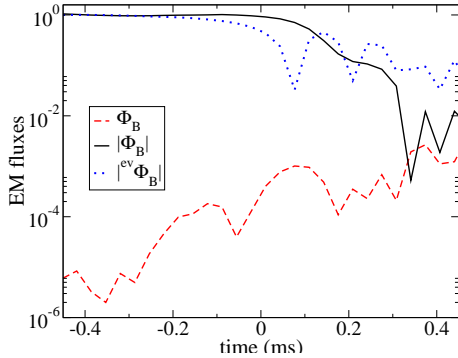


FIG. 17: *Rotating unstable star (force-free)*. The magnetic flux as a function of time, computed at  $r = 1.5R_s$ , normalized with respect to the initial value  $|\Phi_B(t=0)|$ . The unsigned magnetic flux decreases after the black hole formation, similar to the non-rotating case.

run, just as in the non-rotating case, possibly due to the greater self-inductance of the vacuum black hole.

The radiated electromagnetic energy is displayed in Fig. 18, rescaled again with respect to the energy peak in the magnetosphere.

The simulations indicate that around 20% of the energy stored in the magnetosphere is radiated during the collapse in the force-free case, similarly to the electrovacuum case. This is in clear contrast to the non-rotating

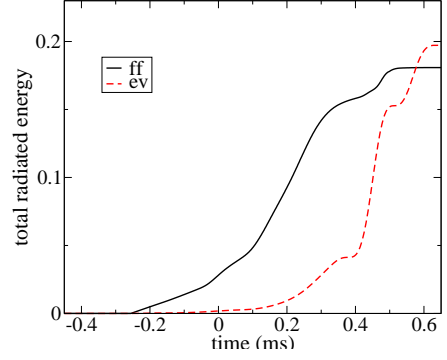


FIG. 18: *Rotating, unstable star*. Time integral of the electromagnetic luminosity, normalized to the peak EM energy of the magnetosphere, in both the force-free and electrovacuum cases. The EM output depends weakly on rotation in the electrovacuum calculations, whereas in the force-free case the output is much larger

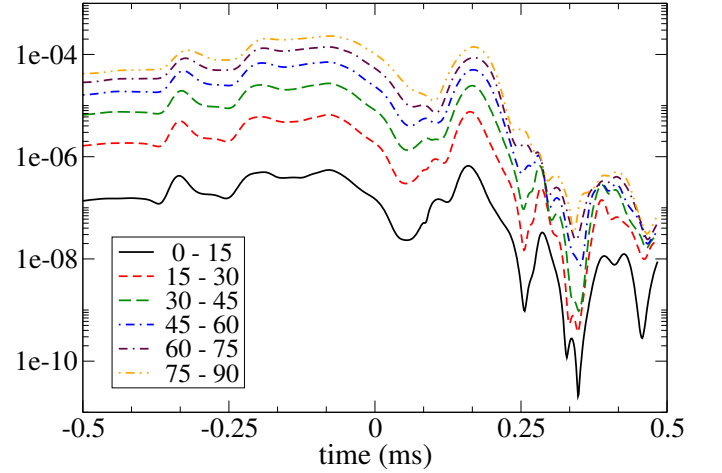


FIG. 19: *Rotating, unstable star (force-free)*. The electromagnetic flux within annuli defined symmetrically in the northern and southern hemispheres by concentric cones having apertures in  $[i15^\circ, (i+1)15^\circ]$  ( $i = 0..5$ ). The highest flux is within  $\theta \in [-50^\circ, 50^\circ]$ . Here, as in the non-rotating case, the radiated energy decays faster than what would be expected from a quasi-normal mode behavior, due to the effects of reconnection.

case, where a much larger energy is radiated in the electrovacuum solution than in the force-free one. We note that although the energy of the magnetosphere is similar in the non-rotating and rotating cases (we find  $C_{\text{peak}} = 1.5$ ), the inclusion of rotation leads to a 20-fold enhancement in the EM energy radiated by a collapsing force-free magnetosphere:  $\epsilon_{\text{rad}} = 0.18$ . Hence Eq. (18) gives  $E_{\text{rad}} \approx 1.3 \times 10^{46} B_{\text{pole},15}^2$  erg, resulting in a strong average luminosity of  $L \approx 1.3 \times 10^{49} B_{\text{pole},15}^2$  erg s $^{-1}$  during the collapse.

The distribution of the radiated energy is essentially

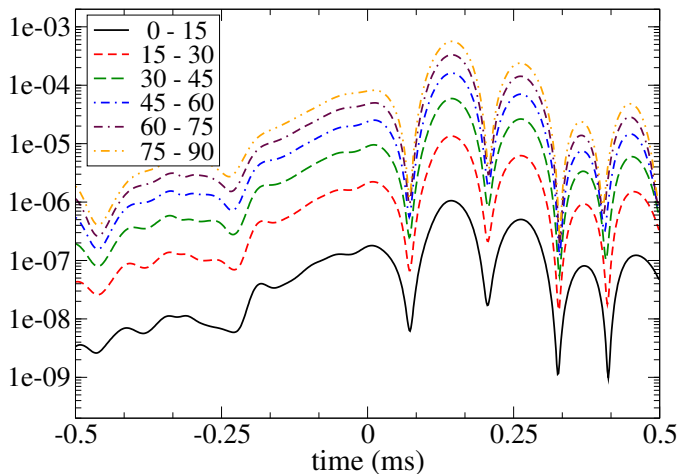


FIG. 20: *Rotating, unstable star (electrovacuum)*. The electromagnetic flux within annuli defined symmetrically in the northern and southern hemispheres by concentric cones having apertures in  $[i15^\circ, (i+1)15^\circ]$  ( $i = 0..5$ ). The radiated energy decays exponentially with a rate consistent with that expected from a quasi-normal mode behavior.

quadrupolar, since the Newman-Penrose scalar  $\Phi_2$  has angular dependence mainly determined by an ( $l = 2, m = 0$ ) mode. This radiation propagates outwards with a velocity  $v = 0.88c$ , which is very similar to what was obtained in the non-rotating case. As displayed in Fig. 19, most of the energy is radiated more efficiently near the angle  $\theta = \pm 50^\circ$  with a peak intensity shortly after the formation of the black hole (For comparison purposes, Fig. 20 illustrates the behavior in the electrovacuum case). Subsequently this emitted radiation fades away rapidly as the magnetic flux is radiated away.

## VII. IMPLICATIONS FOR ASTROPHYSICAL TRANSIENTS: I. GAMMA-RAY BURSTS

We now consider the implications of our simulation results for high-energy transient phenomena. The very luminous gamma-ray bursts (GRBs) are generally believed to result from the formation of a stellar-mass black hole by sudden gravitational collapse, either in the core of a massive star [1, 59], or after the merger of a neutron star with another compact object [2, 3]. A rapidly rotating magnetar is an interesting alternative [60–62]. Our focus here is on ultraluminous EM outflows: the same general mechanism is strongly favored in other contexts such as pulsar synchrotron nebulae [63] and AGN jets [64].

Our calculations focus on the *transition* between a magnetar and a black hole, as a key part of the engine that drives a GRB. The implication is that a build-up of magnetic flux in the surface layers of a rapidly rotating neutron star (formed, e.g., in a binary merger) can driven an electromagnetic outflow during the collapse of

the star, independently of any Blandford-Znajek process operating afterward. As we explain here, this has some advantages over an EM wind operating before the collapse, in that this brief EM transient is likely to be significantly cleaner. We also compare the net EM output with that expected from a post-collapse jet, in the situation where the surface layers of the neutron star, and not the surrounding disk, are the dominant zone for magnetic flux generated by a dynamo process.

Our calculations have revealed strongly dissipative processes at work in the EM field surrounding the collapsing star. These include the reconnection of field lines near the magnetic equator, large-amplitude oscillations in the field, and (in vacuum calculations) the formation of extended zones where  $E^2 \simeq B^2$ , which in the presence of conducting matter imply relativistic motions of the entrained particles transverse to the magnetic field. The ejection of loops of magnetic field is observed in our non-rotating simulations. The dynamical evolution of these loops has interesting implications for the gamma-ray flares from gravitationally stable magnetars (see Sec. VIII).

Although our calculations take into account the presence of plasma implicitly by enforcing  $E \cdot B = 0$ , adding the associated force-free current and enforcing  $|E| < |B|$ , we expect that strong heating will occur in practice. Where the magnetic field reaches  $\sim 10^{15} - 10^{16}$  G, the implied temperature is above  $\sim 1$  MeV. Such a high density of electrons and positrons is created that macroscopic zones of non-vanishing  $E \cdot B$  – as are required by most pulsar discharge models (e.g. [65]) – cannot be maintained. Effective heating can occur by other channels: for example, long-wavelength gradients in the magnetic field are converted efficiently to internal energy if the magnetic field becomes turbulent, so that a wide spectrum of wave motions is formed that extends down to very small scales [66].

The relativistic outflow that is emitted by a rapidly collapsing star should therefore be quite hot. Large-scale magnetic fields and a relativistic photon-electron-positron plasma will both contribute substantially to the energy flux. Magnetar outbursts provide a fairly direct example of this phenomenon.

### A. EM Output Before, During, and After Collapse

The star that collapses to form a black hole passes through three distinct phases: a pre-collapse phase during which it emits a magnetized wind if it rotates; the dynamic collapse phase; and, if an orbiting disk is present – as it is following a neutron star merger – an accretion phase that is accompanied by a relativistic jet. Since our current simulations focus on the intermediate step, it is worth examining its relative contribution to the total EM output of the star.

A large enough EM output  $\Delta E_{\text{collapse}}$  is measured in our rotating force-free simulation to power some short

GRBs, especially if some account is made for beaming. Here the requirement is that the surface magnetic field is strong enough to hold off any accretion flow. At an accretion rate  $\dot{M}$ , this implies a polar magnetic field stronger than [118]

$$B_{\text{pole}} \sim 2 \left[ \frac{\dot{M} V_c(R_{\text{NS}})}{R_{\text{NS}}^2} \right]^{1/2} \sim 7 \times 10^{15} \left( \frac{\dot{M}}{M_{\odot} \text{ s}^{-1}} \right)^{1/2} \text{ G}. \quad (27)$$

Here  $V_c$  is the circular speed, approximated as Keplerian. In this section we take a stellar mass  $M_{\text{NS}} = 2.6 M_{\odot}$  and a radius  $R_{\text{NS}} = 15 \text{ km}$ , as appropriate to a hot and rapidly rotating neutron star. The dipole field energy before the collapse is

$$E_{\text{dipole},0} = \frac{1}{12} B_{\text{pole}}^2 R_{\text{NS}}^3 = 1.5 \times 10^{49} \left( \frac{\dot{M}}{M_{\odot} \text{ s}^{-1}} \right) \text{ erg}. \quad (28)$$

We estimate  $\Delta E_{\text{collapse}} \sim 0.3 E_{\text{dipole},0}$ , given that the energy released is about 0.2 times the peak magnetic energy, which in turn is  $C_{\text{peak}} \sim 1.5$  times  $E_{\text{dipole},0}$ . From Eq. (28) we obtain

$$\Delta E_{\text{collapse}} \sim 5 \times 10^{48} \left( \frac{\dot{M}}{M_{\odot} \text{ s}^{-1}} \right) \text{ erg}. \quad (29)$$

The precise numerical value depends non-linearly on the initial specific angular momentum  $J/M_{\text{NS}}$  through the factor  $\epsilon_{\text{rad}} C_{\text{peak}}$ : faster initial spins imply stronger winding of the magnetic field during the collapse.

The magnetic field of an isolated neutron star acts as a couple between its reservoir of rotational energy and a dissipative outflow. Even in the case of a (gravitationally stable) magnetar, the magnetic energy begins to dominate the rotational energy only at an advanced age, as the star spins down. Therefore the output of the pre-collapse phase could be very large compared with the release of EM energy during the collapse. Comparing the spindown energy radiated over a time  $\Delta t$  with the external magnetic energy (29) gives

$$\frac{L_{\text{sd}} \Delta t}{E_{\text{dipole},0}} = 0.6 \left( \frac{P_{\text{NS}}}{\text{ms}} \right)^{-3} \left( \frac{R_{\text{NS}}}{15 \text{ km}} \right)^3 \left( \frac{\Delta t}{P_{\text{NS}}} \right). \quad (30)$$

Here we have substituted the spindown power of an aligned, force-free rotator [67],

$$L_{\text{sd}} = \frac{1}{4} B_{\text{pole}}^2 R_{\text{NS}}^2 c \left( \frac{\Omega_{\text{NS}} R_{\text{NS}}}{c} \right)^4, \quad (31)$$

where  $\Omega_{\text{NS}} = 2\pi/P_{\text{NS}}$ . An isolated, rotating star would radiate energy equal to  $E_{\text{dipole},0}$  in a few milliseconds..

In the context of binary neutron star mergers, one requires a magnetosphere to emerge from the very strong

shear layer near the surface of the merger remnant (see Section VII B for further discussion of how this could happen). If the neutron star is formed hot, a lengthy pre-collapse spindown phase would cause significant difficulties with the application to short GRBs, because the wind generated during the pre-collapse phase is heavily loaded with nucleons and  $\alpha$  particles that are driven outward by charged-current absorption of electron-type neutrinos near the neutrinosphere [54, 68, 69]. The connection between short GRBs and neutron star mergers would also be disfavored if this pre-collapse outflow lasted longer than  $\sim 300 \text{ ms}$ , given a characteristic short GRB lifetime of 0.03–0.3 seconds [70]. On the other hand, the survival of the merger remnant for  $\sim 100 - 300 \text{ ms}$  would have the advantage of allowing stronger amplification of the magnetic field before the remnant collapses. The possibility of longer-lived merger remnants for some configurations has been raised by recent simulations that employ a realistic, finite-temperature EOS [71].

Although two merging neutron stars are expected initially to have magnetospheres, the torus formed by the tidal disruption of the lighter star has a pressure vastly exceeding that of a typical pulsar dipole. The torus would, therefore, suppress a magnetosphere around the newly formed merger remnant. The neutrino-driven wind that emerges from the polar regions of the remnant will comb out the magnetic field, but this field need not initially be coherent across the star or dynamically important. By the same token, if a torus were entirely absent, then the magnetic field threading the star would dissipate rapidly after the black hole forms, and the post-collapse phase would contribute negligibly to the output of the star.

It is useful to express the EM power in terms of the “open” magnetic flux that connects the surface of the star to the outflowing wind. In the case of an isolated star, this is the flux extending beyond the light cylinder,

$$\Phi_{\text{open}}(\Omega_{\text{NS}}) \simeq \pi B_r(R_{\text{LC}}) R_{\text{LC}}^2 = \Phi_{\text{NS}} \left( \frac{R_{\text{NS}}}{R_{\text{LC}}} \right), \quad (32)$$

where  $\Phi_{\text{NS}} = B_{\text{pole}} \cdot \pi R_{\text{NS}}^2$  is the dipolar magnetic flux threading the star. One can then re-write Eq. (31) as

$$L_{\text{sd}} = \frac{1}{4\pi^2 c} (\Phi_{\text{open}} \Omega_{\text{NS}})^2. \quad (33)$$

After the star forms a distinct magnetosphere, the accretion torus can continue to influence the wind power by modifying the open magnetic flux. Let us suppose that the magnetic pressure dominates the torus ram pressure out to an equatorial distance  $R_A > R_{\text{NS}}$ . Approximating the magnetosphere by a dipole, a fraction

$$\frac{\Phi_{\text{open}}}{\Phi_{\text{NS}}} \sim \frac{R_{\text{NS}}}{R_A} \quad (34)$$

of the stellar flux is trapped by the torus. In this situation, it is still possible for  $\Phi_{\text{open}}$  to exceed Eq. (32),

because the torus can extend inside the stellar light cylinder,

$$\frac{\Phi_{\text{open}}}{\Phi_{\text{open}}(\text{no torus})} \sim \frac{R_{\text{LC}}}{R_A} = 3.3 \left( \frac{R_A}{15 \text{ km}} \right)^{-1} \left( \frac{P_{\text{NS}}}{\text{ms}} \right). \quad (35)$$

During our simulations of the collapse of an isolated star, we observe that the magnetic field lines are strongly twisted, so that most of the closed magnetic flux opens out. Then

$$\Phi_{\text{open}} \rightarrow \Phi_{\text{open}}(\Omega_H), \quad (36)$$

where  $\Omega_H$  is the angular velocity of the horizon.

A torus also plays an important role after the black hole forms by trapping a certain fraction of the magnetic flux that threads the star. If the magnetic field is strong enough to hold off the torus from the star before the collapse, then it will have a similar effect after the collapse. We therefore calculate the Blandford-Znajek power emerging from the horizon by assuming a uniform flux density out to some radius  $R'_A$ . From Eq. (8.65) of [72], one gets,

$$\begin{aligned} L_{\text{BZ}} &\sim \frac{2}{15} \left[ \frac{\Omega_F(\Omega_H - \Omega_F)}{\Omega_H^2} \right] \left( \frac{\Omega_H R_H}{c} \right)^2 R_H^2 \langle B \rangle^2 c \\ &\lesssim \frac{1}{30\pi^2 c} (\Phi_H \Omega_H)^2, \end{aligned} \quad (37)$$

where  $\langle B \rangle$  is the flux density threading the region interior to the torus, and  $\Phi_H = \pi \langle B \rangle R_H^2$ . The difference in the normalizations of Eqs. (33) and (37) largely reflects the fact that the torque on the black hole is maximized when the magnetic field has an angular velocity  $\Omega_F = \Omega_H/2$ .

We can now relate Eq. (37) to the EM power generated before the collapse. The spin angular momentum is approximately conserved during the collapse,  $J \simeq I_{\text{NS}} \Omega_{\text{NS}}$ , and we also set  $M_{\text{BH}} = M_{\text{NS}}$ . Then

$$\frac{J}{GM_{\text{BH}}^2/c} = \varepsilon_I \left( \frac{P_{\text{NS}}}{\text{ms}} \right)^{-1} \left( \frac{R_{\text{NS}}}{15 \text{ km}} \right)^2 \left( \frac{M_{\text{BH}}}{3 M_\odot} \right)^{-1}, \quad (38)$$

where  $\varepsilon_I = I_{\text{NS}}/M_{\text{NS}} R_{\text{NS}}^2 \sim 0.3$ . The angular frequency of the black hole is  $\Omega_H R_H/c = J/M_{\text{BH}} R_{\text{Sch}} = Jc/2GM_{\text{BH}}^2$ , and is related to  $\Omega_{\text{NS}}$  pre-collapse by

$$\frac{\Omega_H}{\Omega_{\text{NS}}} \simeq 0.3 \left( \frac{R_{\text{NS}}}{R_H} \right)^2 \left( \frac{\varepsilon_I}{0.3} \right). \quad (39)$$

where  $R_{\text{Sch}} = 2GM_{\text{BH}}/c^2$  is the Schwarzschild radius. One expects  $\langle B \rangle \sim B_{\text{pole}}$  after the collapse if most of the magnetic flux threading the star is open before the collapse, and the pre-collapse magnetosphere is limited in size. The proportion of the trapped flux threading the hole is

$$\frac{\Phi_H}{\Phi_{\text{open}}} = \left( \frac{R_H}{R'_A} \right)^2 \sim \left( \frac{R_H}{R_{\text{NS}}} \right)^2. \quad (40)$$

We can now show that the EM power is suppressed immediately following the collapse. Substituting equations (39) and (40) into (37) gives

$$\frac{L_{\text{BZ}}}{L_{\text{sd}}} \simeq 0.01, \quad (41)$$

with a coefficient  $(R_A/R_{\text{NS}})^2 (R_{\text{NS}}/R'_A)^4 (\varepsilon_I/0.3)^2$ . Additional power will flow along the magnetic field lines that thread the ergosphere, but this portion of the black hole magnetosphere will mix with the accretion flow and may be less strongly magnetized.

The interesting conclusion here is that the rapid twisting up of the magnetic field during the collapse can generate a larger EM output than a fairly extended jet emission after the collapse. It is worth summarizing the three main sources of this result: i) before the horizon forms, the EM power is proportional to  $\Omega^2$  rather than  $\sim \Omega^2/4$ ; ii) the magnetic flux remains pinned in the star for a few rotation periods during the collapse (before the onset of the black hole), and then springs out to fill a larger volume; and iii) the relation between rotation frequency and angular momentum is enhanced by a factor  $\sim \varepsilon_I^{-1} \sim 3$  prior to the collapse; in other words, relativistic gravity has the effect of softening the growth of the rotation frequency as the star collapses.

A reduction in the trapped flux (due to outward diffusion of the magnetic field into the torus) would, in this situation, initially *increase* the Blandford-Znajek power flowing from the horizon. The pressure of the trapped field approximately balances the ram pressure of the accretion flow at some point outside the horizon. Therefore a reduction in the trapped flux allows the flow to reach closer to the black hole, and attain higher pressures, before being interrupted. Although we are considering the flux originating in a dynamo process before the collapse (Sec. VII B), continued flux generation in the torus by the magnetorotational instability [73] could play a role in modulating the jet power.

### 1. Numerical Comparison

Let us consider the EM energy that would be radiated following a binary NS merger, if the remnant survives long enough to form a magnetosphere (Sec. VII B). Taking  $\Delta E_{\text{collapse}} \sim 0.3 E_{\text{dipole},0}$ , and normalizing to an accretion rate  $0.1 M_\odot \text{ s}^{-1}$  through Eq. (28), gives  $\Delta E_{\text{collapse}} \sim 5 \times 10^{47} \text{ erg}$ . We expect that the gain factor  $\Delta E_{\text{collapse}}/E_{\text{dipole},0}$  depends non-linearly on the pre-collapse rotation rate, since the winding of the magnetospheric field results from a competition between differential rotation and torsional wave motion. In addition,  $\Delta E_{\text{collapse}}$  depends indirectly on the torus mass and pressure through the strength of the magnetic field that is required to hold off the torus material from the neutron star surface. The larger accretion rate in a collapsar environment implies a larger transient energy.



It is possible to make a direct comparison with the Blandford-Znajek jet that follows the collapse, if the magnetic flux that threads the black hole is left behind by the collapsing magnetar. Combining equations (30) and (41), and taking pre-collapse rotation period and radius 0.8 msec and 15 km, one finds that an energy  $\sim 0.3E_{\text{dipole},0}$  would be radiated by a BZ jet over  $\sim 20$  ms. Equivalently, a Blandford-Znajek jet from a  $\sim 3M_{\odot}$  black hole with  $Jc/GM_{\text{BH}}^2 \sim 0.7$  would generate a power (37)  $L_{\text{BZ}} \sim 1 \times 10^{50} B_{15}^2 \text{ erg/s}$ . A recent binary merger simulation with GRMHD and dynamical gravity [74] presented a polar magnetic field  $\sim 7 \times 10^{14} \text{ G}$  developing from a much weaker seed field in the torus. The equation of state used gave a fast collapse to a BH (within  $\sim 10 \text{ ms}$ ), and therefore precluded the surface shear dynamo that we have conjectured. (Note that this polar field could be affected by numerical resistivity, e.g. [75]).

## 2. Baryon Poisoning

Comparing the output  $\Delta E_{\text{collapse}}$  with Eq. (29), one sees that the pre-collapse star would release a comparable energy within  $\sim 100 \text{ ms}$  after forming a magnetosphere. However, it is well known (e.g. [54]) that such an outflow would bear a much higher density of nucleons than a Blandford-Znajek jet from a black hole, due to the absorption of electron-type neutrinos and anti-neutrinos. We expect that this nucleon loading would be strongly suppressed in the dynamical collapse phase, due to i) the relatively short duration of the emission; ii) the strongly wound field geometry ( $B_{\phi}/B_P \gtrsim 5$ ); and iii) redshifting effects. Combining these effects suggests a significant suppression  $\lesssim 0.01 \times 0.1 \sim 10^{-3}$  in the nucleon loading, so that the mass ejected would essentially be that present in the magnetosphere before the collapse.

## B. Emergence of a Magnetosphere via Dynamo Action in a Surface Shear Layer

The immediate aftermath of a binary neutron star merger is distinguished from disk accretion onto a black hole, in that the velocity shear is strongest where the orbiting material makes a transition from centrifugal to hydrostatic support. Another feature which distinguishes the merger remnant from ordinary accreting neutron stars (X-ray pulsars) is that it does not initially have an ordered magnetosphere.

Long after the first stage of the merger is complete, the velocity shear provides a tremendous source of free energy for amplifying a magnetic field. The power dissipated in the material settling onto the neutron star surface is

$$\begin{aligned} L_{\text{shear}} &\sim \frac{1}{2} \dot{M} [V_c^2(R_{\text{NS}}) - \Omega_{\text{NS}}^2 R_{\text{NS}}^2] \\ &\sim 3 \times 10^{52} \left( \frac{\dot{M}}{0.1 M_{\odot} \text{ s}^{-1}} \right) f_{\text{shear}} \text{ erg s}^{-1}, \end{aligned}$$

where  $f_{\text{shear}} \equiv 1 - [\Omega_{\text{NS}} R_{\text{NS}} / V_c(R_{\text{NS}})]^2$ . Note that the surface shear becomes more radially concentrated with time: as differential rotation is erased in the interior of the merger remnant, the surface shear is maintained by continuing accretion. The inner part of the shear layer develops positive  $d\Omega/dr$  and the magnetorotational instability is extinguished.

A strong *feedback mechanism* is present which allows rapid magnetic field growth, but causes this growth to saturate once the star is able to form a magnetosphere that holds off the accretion flow. When the magnetosphere is present, the accreting material follows the magnetic field and reaches the star at the same angular velocity. Shearing of the magnetic field in the outer layers of the star is therefore turned off. This effect is clearly demonstrated in the 3D accretion simulations of [82].

Only a tiny fraction of the accretion energy  $L_{\text{shear}} \Delta t$  must be converted to a poloidal magnetic field to hold off the accretion flow: substituting (27) into the dipole energy (28) gives

$$\begin{aligned} \frac{E_{\text{dipole}}}{L_{\text{shear}} \Delta t} &= \frac{2}{3 f_{\text{shear}} \Delta t} \left( \frac{R_{\text{NS}}^3}{GM_{\text{NS}}} \right)^{1/2} \\ &= 6 \times 10^{-4} \left( \frac{\Delta t}{100 \text{ ms}} \right)^{-1} f_{\text{shear}}^{-1}. \end{aligned} \quad (43)$$

over a duration  $\Delta t$ .

Low-mass X-ray binaries provide a nice example of systems where this feedback appears to operate. The millisecond radio pulsars that are descended from them have magnetic fields that are just strong enough ( $B \sim 10^8 - 10^9 \text{ G}$ ) to hold off an Eddington-level accretion flow onto a neutron star – but not much stronger. The absence of persistent pulsations in the majority of LMXBs then requires that the magnetic field be aligned with the angular momentum of the accretion flow.

Now let us consider how the magnetic field evolves in the surface shear layer. The field present initially in the merging stars is rapidly amplified by a Kelvin-Helmholtz instability [28, 75], or the magnetorotational instability [73]. Rapid growth of the magnetic field on large scales is sensitive to the speed of magnetic reconnection in the fluid, and requires three-dimensional motions. The two-dimensional wrapping of a magnetic field by Kelvin-Helmholtz vortices does not generate net flux; and the initial growth length of the MRI is very small compared with the scale height of the torus. MRI growth is fastest on a scale  $k^{-1} \sim B/(4\pi\rho)^{1/2}\Omega \sim 10^{-4}(B/10^{12} \text{ G})r$  in a torus of mass  $\sim 0.01 M_{\odot}$  [73].

The hydrostatic structure of the inner shear layer makes it easier for the magnetic field to be pinned and retained than it would be in the surrounding torus. The magnetic field threading the shear layer is wound up, and since  $d\Omega/dr > 0$ , the mean toroidal flux density grows at least in a linear manner. If a hot, rotating, and massive neutron star ( $M_{\text{NS}} \sim 2.6 - 3 M_{\odot}$ ) can survive collapse for

more than  $\sim 100$  ms, as is suggested by recent simulations of [71], then this toroidal field becomes quite strong. Even if the seed poloidal field is as weak as  $B_{P,0} \sim 10^{13}$  G – within the range of pulsar fields – then the toroidal field reaches

$$\begin{aligned} B_\phi &\sim [\Omega_c(R_{\text{NS}}) - \Omega_{\text{NS}}] \Delta t B_{P,0} \\ &= 1 \times 10^{16} \left( \frac{\Delta t}{100 \text{ ms}} \right) \left( \frac{\Omega_c(R_{\text{NS}}) - \Omega_{\text{NS}}}{10^4 \text{ s}^{-1}} \right) \\ &\quad \times \left( \frac{B_{P,0}}{10^{13} \text{ G}} \right) \text{ G}. \end{aligned} \quad (44)$$

Here  $\Omega_c(R_{\text{NS}})$  is the angular frequency at the surface of the torus.

Exponential magnetic field growth becomes possible when the wound-up field can rise buoyantly through the shear layer. The large dissipated power (42) will generate a strongly positive entropy gradient in the inner part of the shear layer. Where the material is convectively stable, only magnetic fields stronger than  $\sim (GM_{\text{NS}} M_{\text{shear}} / R_{\text{NS}}^4)^{1/2} \sim 1 \times 10^{17} (M_{\text{shear}} / 0.1 M_\odot)^{1/2}$  G can directly overcome the pressure of the overlying material. But even in this case, the intense flux of electron-type neutrinos allows a magnetic field stronger than  $\sim 10^{15}$  G to rise buoyantly on the Alfvén timescale, by erasing gradients in entropy and electron fraction that impede buoyancy [83]. The buoyancy time is  $t_A \sim \ell_P (4\pi\rho)^{1/2} / B_\phi \sim 1 (B_\phi / 10^{16} \text{ G})^{-1} (\rho / 10^{14} \text{ g cm}^{-3})^{1/2}$  ms across a pressure scale height  $\ell_P \sim R_{\text{NS}} / 4 \sim 3 - 4$  km. Thus an exponential feedback loop appears quite likely in this situation.

One observes that the large-scale dipole magnetic field that emerges may be sensitive to the seed magnetic field, in the sense that a *minimal* seed field is required for the linearly wound field to reach the buoyancy threshold. Nonetheless, it is also clear that magnetar-strength magnetic fields do not require magnetar-strength seed fields in the presence of persistent surface shear.

The strength of the magnetosphere that eventually emerges results from a competition between the finite rate of amplification and the diminishing shear stress at the surface of the star. At an age of  $\sim 10(100)$  ms, a poloidal magnetic field stronger than  $\sim 10^{16}$  G ( $10^{15}$  G) will begin to apply a strong, negative feedback on the surface shear. Once the torus mass drops to the point that accretion is mediated mainly by magnetic stresses, the accretion rate is  $\dot{M}_0 \sim M_{T,0} / t_{\text{diff},0} \sim 10 (\alpha / 0.1) (M_{T,0} / 0.1 M_\odot) M_\odot \text{ s}^{-1}$ . Here  $M_{T,0}$  and  $t_{\text{diff},0} \sim 10 (\alpha / 0.1)^{-1}$  ms are the initial torus mass and diffusion time in this viscous phase, and  $\alpha$  is the viscosity coefficient. The accretion rate drops as the torus material spreads outward, as  $\dot{M} \sim \dot{M}_0 (t / t_{\text{diff},0})^{-4/3}$ , as long as the torus remains geometrically thick and conserves its angular momentum (e.g. [84]).

### C. Galactic Magnetars and Delayed Collapse

We now consider the observational imprint of a magnetar if it forms by the accretion of a thin layer of strongly sheared material, but is (initially) gravitationally stable. We focus on the rate of energy loss and the spin history of the star.

There is a substantial reduction in the energy release by spindown, compared with a star that initially rotated as a solid body, due to the internal rearrangement of angular momentum. Approximate solid-body rotation is attained on the poloidal Alfvén timescale  $R_{\text{NS}} (4\pi\rho)^{1/2} / B_{\text{pole}}$ , which is generally much shorter than the magnetic-dipole spindown time

$$t_{\text{sd}} = \frac{I_{\text{NS}} P_{\text{NS}}^2 c^3}{2\pi^2 B_{\text{pole}}^2 R_{\text{NS}}^6}. \quad (45)$$

Most of the shear energy is then dissipated *internally*.

A delayed collapse is possible if the magnetar only slightly exceeds the maximum mass for a non-rotating, zero-temperature neutron star. The loss of rotational support by a magnetic wind would trigger a collapse on the rotational braking time.

Quite generally, the accretion of a thin layer of strongly sheared material provides an attractive mechanism for creating magnetars, and so the results of this section should have a broader application to the Galactic magnetar population, even if these stars are well below the maximum mass. Several possible channels are available: the rotation of the accreting material could be generated by an instability of the supernova shock [85–88]; or the neutron star could be exposed to material with very strong vorticity in a merger event, e.g. when it merges with a companion CO white dwarf, or with the core of an evolving Be star.

The spindown power that is released by the magnetar is then reduced significantly compared with a star which rotates uniformly with the same angular velocity as the surface material. The final spin period resulting from the accretion of a layer of mass  $M_{\text{shear}}$  and rotation period  $P_{\text{shear}}$  onto a neutron star of total mass  $M_{\text{NS}}$  is

$$\begin{aligned} P_{\text{NS}} &= \left[ \frac{(2/3) M_{\text{shear}} R_{\text{NS}}^2}{I_{\text{NS}}} \right]^{-1} P_{\text{shear}} \\ &= 10.5 j_{\text{shear}}^{-1} \left( \frac{M_{\text{NS}}}{2 M_\odot} \right) \text{ ms}, \end{aligned} \quad (46)$$

where  $j_{\text{shear}} \equiv (M_{\text{shear}} / 0.1 M_\odot) (P_{\text{shear}} / \text{ms})^{-1}$ . As the star spins down, it deposits a rotational energy

$$\frac{1}{2} I_{\text{NS}} \Omega_{\text{NS}}^2 = 2.5 \times 10^{50} j_{\text{shear}}^2 \left( \frac{M_{\text{NS}}}{2 M_\odot} \right)^{-1} \left( \frac{R_{\text{NS}}}{10 \text{ km}} \right)^2 \text{ erg} \quad (47)$$

in the surrounding shock wave. For a magnetar of polar field  $B_{\text{pole}}$ , the corresponding spindown luminosity is fairly modest,

$$L_{\text{sd}} = 1.4 \times 10^{45} \left( \frac{B_{\text{pole}}}{10^{15} \text{ G}} \right)^2 \left( \frac{P_{\text{NS}}}{10 \text{ ms}} \right)^{-4}$$



$$\times \left( \frac{R_{\text{NS}}}{10 \text{ km}} \right)^6 \text{ erg s}^{-1}, \quad (48)$$

and the star enters the extended spindown phase after a time

$$t_{\text{sd}} = 2 \left( \frac{B_{\text{pole}}}{10^{15} \text{ G}} \right)^{-2} \left( \frac{P_{\text{NS}}}{10 \text{ ms}} \right)^2 \left( \frac{M_{\text{NS}}}{2 M_{\odot}} \right) \times \left( \frac{R_{\text{NS}}}{10 \text{ km}} \right)^{-4} \text{ day}. \quad (49)$$

In this situation, only a very strong internal magnetic field ( $B_{\text{toroidal}} \gtrsim 10^{17} \text{ G}$ ) would induce sufficient triaxiality in the star that the gravity wave torque competed with the external electromagnetic torque [89].

### VIII. PLASMOID DYNAMICS AND RADIATION: IMPLICATIONS FOR MAGNETAR FLARES

Escaping loops of magnetic field are observed in our non-rotating simulations. These loops are formed by magnetic reconnection, which means their size and rate of formation are sensitive to the treatment of resistivity, and to the disregard of stresses associated with bulk plasma flow by the adoption of the force-free equations. An outgoing plasmoid (containing plasma and a closed magnetic field) has a well-defined center of mass: we find that its bulk motion is measurably smaller than the speed of light,  $V_{\text{bulk}} \sim 0.9c$  and  $\Gamma_{\text{bulk}} \sim 2$ , at a distance  $r \sim 10$  times the pre-collapse neutron star radius  $R_{\text{NS}}$ . This is significantly less relativistic than the bulk motion expected for a gas of freely expanding particles released by the collapsed star ( $\Gamma_{\text{bulk}} \gtrsim r/R_{\text{NS}} \sim 10$ ).

After addressing each of these issues, we make contact with the giant gamma-ray flares of the Galactic magnetars. These appear to involve the ejection of an energetic plasmoid ( $\sim 10^{44} - 10^{46} \text{ erg}$ ), but due to the shearing of the magnetic field lines rather than the collapse of the star [90].

#### A. Dependence of Reconnection Rate on Resistivity Model

When magnetic field lines of an opposing sense are stretched out and forced into contact, the rate at which they reconnect is sensitive to the microscopic model of resistivity. In an ohmic plasma with a uniform resistivity, a long current sheet forms and reconnection is very slow; fast reconnection with an x-point geometry depends on a local maximum in the resistivity [91]. In some contexts, such as the Solar corona, the microscopic explanation for this behavior may be provided by the Hall terms in the conductivity [92]. These are relatively less important if the plasma is loaded with  $e^+/e^-$  pairs, as would be expected in the magnetosphere of a collapsing magnetar. In

a fluid, small-scale hydromagnetic turbulence appears to greatly accelerate the reconnection rate [93]; but whether such a process can operate in a low- $\beta$  plasma of astrophysical dimensions is not yet determined.

In the present work we find evidence for relatively fast reconnection of magnetic field lines,  $V_{\text{rec}} \sim 0.1 c$ , as calculated in the force-free approximation (Sec. VIA). This results from a change in topology of the field lines (the formation of an x-point). It is not due to strongly enhanced dissipation in an extended equatorial current sheet:  $E \cdot J$  dissipation is measured to be small in both the rotating and non-rotating cases. Such a concern arises in force-free calculations of pulsar magnetospheres, where the magnetic field is less dynamic and is anchored in the star. There the absence of fluid pressure support in the current sheet leads to a rapid collapse of the magnetic field toward the sheet, unless explicitly compensated [8, 9]. In the present case, after the black hole forms the inflow of magnetic flux toward the equator can continue in a more dynamic manner into the star, or out to the computational boundary.

A recent treatment of reconnection in the magnetosphere of a stationary black hole [57] illustrates a slower field decay when employing an ideal MHD treatment, as compared to a force-free approach. (Resistivity in the MHD case arises through the numerical approximation.) Such a slower decay is also observed at late stages after the formation of the black hole in our simulations when comparing force-free and ideal MHD fields [119]; though by this time the field strengths are orders of magnitude below their peak values. A comparison of force-free and MHD reconnection calculations which explores more general resistivity models, and their influence on the reconnection geometry, remains to be developed.

#### B. Magnetic Reconnection Delayed by Plasma Outflow

Reconnection is usually studied in a context where the plasma flow speed along the magnetic field is a small fraction of the Alfvén speed: for example, in a steady MHD wind, the conservation of angular momentum implies a slow drift of particles along the spiral magnetic field outside the Alfvén critical point. However, in some contexts, such as magnetar flares, the flow speed can approach the speed of light. Similarly, in our collapse simulations we see large-amplitude motions on the magnetic field loops threading the neutron star, which suggest strong plasma heating. The backreaction of the outflowing plasma on the reconnection of field lines is not taken into account.

Even when the magnetic field has a tendency to reconnect through an x-point, reconnection will be *delayed* until the kinetic pressure  $\sim U\beta^2$  of the outflowing pair-photon plasma (with thermal energy density  $\sim U$ ) drops below the Poynting flux that would flow toward the cur-

rent sheet in the absence of plasma flow. One requires

$$U\beta^2 \lesssim 0.1 \frac{V_A}{c} \frac{B^2}{8\pi}, \quad (50)$$

where the coefficient on the right-hand-side is appropriate for fast x-point reconnection.

The magnetic field lines are stretched outward by the plasma flow beyond an Alfvén radius [66]

$$\begin{aligned} \frac{R_A}{R_{\text{NS}}} &= \left( \frac{B_{\text{pole}}^2 R_{\text{NS}}^2 c}{4L_\gamma} \right)^{1/4} \\ &= 16 \left( \frac{B_{\text{pole}}}{10^{15} \text{ G}} \right)^{1/2} \left( \frac{L_\gamma}{10^{47} \text{ erg s}^{-1}} \right)^{-1/4} \end{aligned} \quad (51)$$

given  $R_{\text{NS}} \sim 10$  km. Note that, at the peak of the outflow, the pressure of the pair-photon fluid is comparable to the pressure of the stretched magnetic field lines at  $r = R_A$ , and outside this radius grows as  $\sim (r/R_A)^2$  with respect to the split-monopole field pressure. For example, in a magnetar giant flare, the  $\sim 0.1$  s width of the main gamma-ray pulse is comparable to the time for magnetic and elastic stresses to rearrange the stellar interior; but it is  $\sim 300$  times longer than the flow time out to the Alfvén radius (51), and therefore much longer than the timescale for x-point reconnection at a speed  $\sim 0.1c$ .

### C. Radio Afterglow from Strongly Magnetized Outflows

A magnetically-dominated plasma that is ejected from a collapsing magnetar (or a nearby Soft Gamma Repeater) can be a much stronger source of synchrotron emission than a shocked plasma of comparable energy density. Existing calculations of radio afterglows of short GRBs ([94] and references therein), as well as calculations of the radio afterglow of SGR giant flares [95], focus on synchrotron emission by a population of non-thermal electrons that are accelerated at a shock that leads the outflow. For the bulk of GRBs, one infers efficiencies of conversion  $\varepsilon_e, \varepsilon_B \sim 0.1$  of bulk kinetic energy to non-thermal electrons and to magnetic fields downstream of the forward shock. These moderate values of  $\varepsilon_e$  and  $\varepsilon_B$  are consistent with the broadband tails of radio-X-ray emission that follow the brief, bright gamma-ray phase.

The synchrotron emission from a magnetically-dominated plasmoid will be proportionately much brighter, by up to a factor  $\sim 100$ , for two reasons. First, and most obviously,  $\varepsilon_B$  now approaches unity. Second, if the magnetic energy density dominates the thermal energy density, then a cascade process (involving the creation of high-wavenumber Alfvén modes) preferentially heats the electrons [96]. If the plasma is very relativistic, damping is mainly due to charge-starvation of the waves, at wavenumbers where the amplitude of the fluctuating

current density begins to exceed  $en_e c$  [66, 77]. (A different damping mechanism operates at higher ion densities: the waves are Landau-damped on the parallel motion of the electrons.) In practice, the relative amplitudes of the bulk synchrotron emission and the shock emission will depend on the degree of disorder in the plasmoid magnetic field. But for magnetar flares, indirect evidence that bulk synchrotron emission dominates comes from a rapid initial drop in radio flux that is consistent with the sudden compression of the plasmoid, followed by rapid adiabatic cooling [95].

### D. Applications to Magnetar Outbursts

Magnetar outbursts involve more limited releases of energy that leave the original star intact. They are triggered when the footpoints of a  $\sim 10^{15}$  G magnetic field are strongly sheared by an elastic instability of a neutron star crust, thereby generating a hot plasma and an intense burst of gamma-rays [90, 97]. The first, extremely bright, stage of a giant magnetar flare lasts only  $\sim 100$  ms and bears a considerable resemblance to a ‘classical’ gamma-ray burst, demonstrating high temperatures ( $kT \gtrsim 200$  keV) and a significant non-thermal component to the spectrum [98]. (This phase saturates almost all X-ray detectors, but was well-resolved by the Geotail experiment [99] in the 27 August 1998 and 27 December 2004 flares.) The duration and luminosity are consistent with the internal rearrangement of the magnetic field in a neutron star, with a strength  $\sim 4\text{--}5 \times 10^{15}$  G based on considerations of magnetic field transport and global flare energetics [100], several times stronger than the standard dipole expression for the spindown-derived magnetic field.

The giant flares appear to involve the ejection of a plasmoid. The combination of fast variability and extreme luminosity (up to  $\sim 10^{48}$  ergs s $^{-1}$ ) implies, through the usual arguments of gamma-ray opacity [101], that the emitting plasma has expanded to a much larger volume than that of the neutron star. This expanding plasma is an excellent electrical conductor and must carry some of the stellar magnetic field with it.

This expected property of magnetar giant flares helps to explain two apparently contradictory phenomena. A straightforward argument based on the theory of thermal fireballs (e.g. [102]) shows that the expanding plasma is moving with a high Lorentz factor at the radius ( $\gtrsim 10^8$  cm) where it becomes transparent to the gamma-rays [97]. The observation of variability on a timescale  $\delta t_{\text{var}} \sim 4\text{--}20$  ms in the gamma-ray flux implies strong constraints on the baryon rest energy flux. The advected electrons and ions must become transparent to the gamma-rays close enough to the magnetar that the differential light-travel time  $r/2\Gamma^2 c$  across the outflowing plasma is shorter than  $\delta t_{\text{var}}$ . Given a total outflow luminosity  $L$ , this implies that the ion rest energy contributes no more than a

fraction

$$\begin{aligned} \frac{\dot{M}c^2}{L} &< \left( \frac{16\pi m_p c^4 \delta t_{\text{var}}}{L\sigma_T} \right)^{1/5} \\ &= 0.1 \left( \frac{\delta t_{\text{var}}}{10 \text{ ms}} \right)^{1/5} \left( \frac{L}{10^{47} \text{ erg s}^{-1}} \right)^{-1/5} \end{aligned} \quad (52)$$

of the energy flux.

On the other hand, radio monitoring detected transient emission in the weeks following both flares [103, 104]. The emission following the 2004 flare was especially bright, as befitting the much greater energy of the burst, and could be tracked on the sky for more than a year. The expansion of the radio source implies a transverse velocity  $v \sim 0.7(D/15 \text{ kpc})c$  [104]. After this, clear evidence is seen for a break in the radio light curve consistent with a transition from uniform expansion to a Sedov-like phase. We infer that the measured proper motion is probably the free expansion velocity, as corrected for relativistic aberration.

In principle it is possible for the measured transverse speed to be less than the speed of light, if the intrinsic motion  $V$  is nearly luminal but the motion is directed away from the observer (at some angle  $\theta > \pi/2$  with respect to the line of sight to the magnetar):  $\beta_{\perp, \text{obs}} = \beta \sin \theta / (1 - \beta \cos \theta)$ . The observed relative brightness of both the radio and gamma-ray emission argues against this: one measures  $E_\gamma \sim 4 \times 10^{44} (D/15 \text{ kpc})^2$  in 2004 vs.  $E_\gamma \sim 5 \times 10^{46} (D/15 \text{ kpc})^2$  in 1998, and a radio flux  $F_\nu \sim 50 \text{ mJy}$  vs.  $0.3 \text{ } \mu\text{Jy}$  at 8.5 GHz 1 week after the flare [99, 103, 105]. (A factor  $\sim 2$  underestimate of the  $\sim 15 \text{ kpc}$  distance to SGR 1806-20 appears unlikely given that the source position is in the Galactic plane.)

The energy reservoir that powers the early, subluminal stage of the radio afterglow must be composed of something other than electrons and positrons emitted by the star, which would mainly have annihilated during the very brief fireball phase. A reconnected magnetic field is the most plausible delayed carrier of energy, especially given the strong limitations on the baryon flux during the  $\lesssim 100 \text{ ms}$  gamma-ray pulse. A closed loop of magnetic field carries a finite inertia, and so its center-of-mass frame will not accelerate with distance from the source as does that of a collimated particle beam.

The outflowing pair-photon fluid must overcome the tension of the magnetic field lines that are anchored in the star, and so comparable energy can be put into the stretched field, which is pulled into a split-monopole configuration. The energy of the stretched field is concentrated close to the star,  $B^2 r^3 \sim r^{-1}$ , although not as strongly concentrated as in a static dipole ( $B^2 r^3 \sim r^{-3}$ ). In a static plasma, the time for reconnection at the Alfvén radius  $R_A$  is  $t_{\text{rec}} \sim 3(R_A/100 \text{ km})(V_A/0.1 c)^{-1} \text{ ms}$ . Comparing this expression with the measured e-folding time of  $\sim 30 \text{ ms}$  for the tails of the giant flare pulses [99] suggests that reconnection is gated by the decrease in pair-photon pressure.

We conclude that, in a magnetar giant flare, most of

the released magnetic energy tends to *follow* the pair-photon pulse, with the delay between the two components being due to continued shearing of the external magnetic as the interior of the magnetar adjusts on the internal Alfvén time of  $\sim 0.1 \text{ s}$ .

## IX. CONCLUDING REMARKS

Understanding the global behavior of strongly gravitating, dynamical systems, containing dense matter coupled to ultra-strong magnetic fields, is of key importance for a thorough understanding of possible signals from them. In this work, we have presented a new approach to this end by combining the ideal MHD and force-free approximations in a suitable manner within general relativity.

We expect that this hybrid scheme represents real progress towards greater realism. The stellar interior utilizes ideal MHD to faithfully model the neutron star without the disadvantages incumbent in the low density exterior. Likewise, the exterior solution uses the force-free approach and so captures the dynamics of the tenuous plasma. The entire domain is described by a fully nonlinear and fully dynamic general relativity solution necessary for strong-field gravity. Indeed, a key aspect of this approach is its generality. It does not require a prescribed stationary stellar boundary, and can be applied, for example, to dynamical systems such as collapsing stars and non-vacuum compact binaries.

We have exploited this approach to study stellar collapse in both rotating and non-rotating cases. Our studies reveal a rich phenomenology in the magnetosphere as the collapse proceeds. In particular, magnetic reconnection plays an important role by inducing strong electromagnetic emission as well as the infall of electromagnetic energy into the black hole, which in a short time loses all its ‘hair’. When the star starts off rapidly rotating, the energy of the magnetospheric plasma grows significantly during the collapse. As the star rotates faster, its magnetic field lines do not have time to re-adjust to the increased rotation, and are strongly wound up out to the initial light cylinder. It is worth emphasizing that this conversion of dynamical energy into electromagnetic energy does not depend on resistive effects.

Two issues of principle have arisen in performing these calculations. First, we have shown conclusively that the force-free approximation to the evolution of a dilute, relativistic plasma inevitably leads to singularities. These singularities are avoided in our calculations by continuously pruning the electric field. In the simulations that we have run, this procedure appears to cause limited energy dissipation, but its necessity should be kept in mind.

The second issue of principle regards the dependence of the reconnection geometry on the resistivity model. Fluid pressure is responsible for slowing down the rate of reconnection unless an x-point geometry is able to form. By neglecting fluid pressure, the force-free approxima-

tion clearly facilitates the formation of x-points. In spite of this, we observe very limited numerical dissipation in current sheets. Although the plasma that is represented by our model magnetospheres is, in reality, strongly collisional, it should be kept in mind that fast x-point reconnection still occurs in collisional plasmas in the presence of hydromagnetic turbulence – as has been demonstrated so far in weakly magnetized plasmas [93]. Some further exploration of the reconnection geometry is possible in resistive MHD calculations of stellar collapse by varying the spatial dependence of the resistivity.

We have also discussed how the electromagnetic outbursts from collapsing magnetars may have interesting observational effects. In particular, our results are relevant to binary neutron star merger scenarios, in which a hypermassive neutron star forms and collapses to a black hole. Collapse to a black hole can happen either promptly or after many dynamical times, depending on the masses involved and the equation of state describing the stars (see, for instance, [19]). Although Kelvin-Helmholtz and magnetorotational instabilities will create ultrastrong magnetic fields ( $\gtrsim 10^{14-16}$  G), we have suggested that the global field (in particular, the amount of magnetic flux threading the merger remnant and eventual black hole) could depend strongly on the lifetime of the remnant. The formation of a distinct magnetosphere would require tapping only  $\sim 10^{-3} - 10^{-4}$  of the energy dissipated in shear layer at the remnant surface. As such a star collapsed, the magnetosphere would qualitatively follow the behavior outlined here. The electromagnetic output of the collapse could compete with the later emission from a Blandford-Znajek jet emanating from the black hole horizon, and source a powerful electromagnetic counterpart to the gravity wave signal (e.g. [106]). In addition, the magnetic field dynamics that is revealed in our simulations has a number of interesting implications for gamma-ray bursts and magnetar flares, as discussed in Secs. VII and VIII.

Beyond the work analyzed here, our approach is readily applicable to other relevant systems and will be applied, in particular, to study binary neutron star systems [107], and black hole-neutron star systems (see e.g. [108]). It is important to stress, however, that our approach is not free of ambiguities, in particular with respect to how and where the matching between the force-free and ideal MHD regions is implemented. To the extent possible, we have tested the robustness of our results versus known solutions, which give us confidence in this approach.

**Acknowledgments:** It is a pleasure to thank P. Goldreich for insights and discussions during the course of this work. We also thank E. Berti, P. Cerda-Duran, J. McKinney, R. O’Shaughnessy, E. Ramirez-Ruiz, E. Quataert, A. Spitkovsky and D. Tsang as well as our long time collaborators M. Anderson, E. Hirschmann, P. Motl, D. Neilsen and O. Reula, for discussions and comments. This work was supported by the NSF (PHY-0969827 to Long Island University) and NSERC through Discovery Grants (to CT and LL). Research at Perimeter

Institute is supported through Industry Canada and by the Province of Ontario through the Ministry of Research & Innovation. Computations were performed at Teragrid and Scinet.

## Appendix A: The Transition from Ideal to Force-Free MHD

Details of the transition from the ideal MHD regime to the force-free regime merit particular attention, especially in our rotating collapse solutions. Since we match two different formulations of Maxwell’s equations coupled to conducting matter, it is important to understand how the choice of matching layer affects the exterior force-free solution. Of course, an unambiguous test can only be provided by a complete resistive MHD solution that can handle the strongly magnetized regions outside the star and, in particular, can follow the large changes in density and rotation that are encountered during the collapse. While work on this direction is in progress, the simpler approach presented here allows us to obtain a first solution to the relativistic magnetosphere in this strongly dynamic situation.

The positioning of the matching zone is constrained by competing considerations. On the one hand, if it sits too close to the surface, then the interior MHD solution that sources the exterior force-free solution will be unrealistic, due to the density floor that is applied in the MHD atmosphere. One thus might want to place the transition layer well within the stellar surface. However, such a deep layer might underestimate the magnetic field strength at the base of the magnetosphere, and imply force-free behavior of the magnetic field where that approximation is not justified.

In particular, we have found that placing the transition zone at too low a density implies an unrealistically large toroidal magnetic field at the base of the force-free zone. Recall that the region exterior to the star, with its tenuous plasma, will have a relatively large magnetization, and should be forced to co-rotate with the interior of the star. Unless prohibitively high resolution is employed, the atmosphere of the MHD solution has a large enough inertia that this condition can be violated. Instead, the magnetic field experiences a non-negligible (and non-physical) differential rotation. This effect is easily exacerbated in a collapsing solution.

Within our current approach, we address these issues in two ways, by (i) adopting an initial configuration of the force-free fields and ideal MHD fields respecting such co-rotation up to the light cylinder and with a suitable differential rotation outside that radius; and (ii) choosing a transition layer at an appropriate distance inside the stellar surface.

Regarding the initial data, since the rotation induces a toroidal magnetic field we adopt initial data that has a toroidal magnetic defined as  $B_\phi = -\Omega_F R_{\text{cyl}} B_r$  and also  $E = -v \times B$  throughout domain. We also choose the

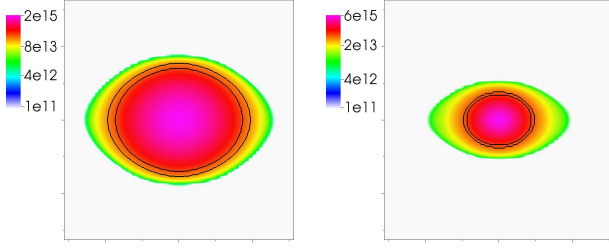


FIG. 21: *Rotating, unstable star (force-free)*. Isosurfaces of the kernel function of Eq. (9) at two different times  $t = -0.30\text{ms}$ , left, and  $t = -0.07\text{ms}$ , right, while the rotating star collapses. Mapped in color is the density of the star in cgs units in a equatorial plane. Black lines mark two isosurfaces of the kernel function, corresponding to  $F = (0.01, 0.99)$ .

MHD atmosphere to co-rotate with the star for  $R_{\text{cyl}} < 2R_{\text{star}}$ , and not to rotate otherwise.

Both the location of the stellar surface and the density in the transition layer are dynamical. It is important that the choice of transition density  $\rho^{\text{match}}$  in Eq. (9) respects the increasing density of the collapsing star. In order to maintain a consistent depth of the transition layer, its position is adjusted as the star collapses by scaling the matching density  $\rho^{\text{match}}$  in proportion to the peak density within the star:  $\rho^{\text{match}}(t) = \rho^{\text{match}}(t = 0)[\rho_{\text{max}}(t)/\rho_{\text{max}}(t = 0)]$ . The transition layer is displayed at the beginning and near the end of the collapse in Fig. 21. Notice that with this conservative approach we are underestimating possible rotational effects.

The angular frequency  $\Omega_F$  of magnetic field lines anchored near the rotation axis of the star is illustrated in Fig. 22. From the initial condition (in which constancy of  $\Omega_F$  is enforced), a negative gradient in  $\Omega_F$  develops in the transition layer during the earliest stages of the collapse. This negative gradient has then disappeared by the time that the stellar angular velocity has increased by  $\sim 20\%$  above the initial value  $\Omega_0$  (see Fig. 14). From then on, the qualitative behavior obtained is consistent with the expected one: during the collapse, the star transfers angular momentum to the magnetic field

lines so that  $\Omega_F = \Omega_{\text{star}}$  near its surface, propagating along the magnetic field lines with a speed  $\sim c$ .

The sharp negative gradient appearing in the last stages of the collapse reflects the strong radial gradient in  $\Omega_{\text{star}}$  that appears near the rotation axis, as well as the onset of strong general relativistic effects. As the event horizon arises (prior to the formation of the apparent horizon at  $t = 0$ ), it disconnects the interior from the exterior solution and causes  $\Omega_F$  to decrease, tending to

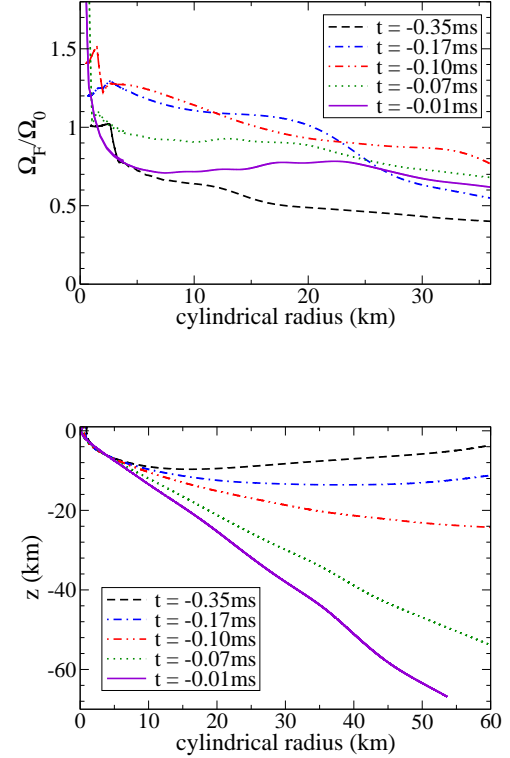


FIG. 22: *Rotating, unstable star (force-free)*. (Top panel) Angular velocity  $\Omega_F$  of the magnetic field line emanating from  $\theta = 122^\circ, \phi = 0^\circ$  as a function of cylindrical radius (normalized with respect to its initial value). (Bottom panel) Shape of such magnetic field line as time progresses.

the value  $\Omega_F = \Omega_H/2$  expected by the Blandford-Znajek solution of a spinning black hole.

- 
- [1] S. E. Woosley, *Astroph. J.* **405**, 273 (1993).
  - [2] D. Eichler, M. Livio, T. Piran, and D. N. Schramm, *Nature* **340**, 126 (1989).
  - [3] R. Narayan, B. Paczynski, and T. Piran, *Astroph. J.* **395**, L83 (1992), arXiv:astro-ph/9204001.
  - [4] C. Thompson, *Mon. Not. R. Astron. Soc.* **270**, 480

- (1994).
- [5] P. Meszaros and M. J. Rees, *Astroph. J.* **482**, L29 (1997), arXiv:astro-ph/9609065.
- [6] J. C. McKinney, *Mon. Not. R. Astron. Soc.* **368**, 1561 (2006), arXiv:astro-ph/0603045.
- [7] I. Contopoulos and A. Spitkovsky, *Astrophys. J.* **643**,

- 1139 (2006), arXiv:astro-ph/0512002.
- [8] A. Spitkovsky, *Astrophys. J.* **648**, L51 (2006), astro-ph/0603147.
  - [9] J. C. McKinney, *Mon. Not. Roy. Astron. Soc.* **367**, 1797 (2006).
  - [10] B. C. Stephens, M. D. Duez, Y. T. Liu, S. L. Shapiro, and M. Shibata, *Class.Quant.Grav.* **24**, S207 (2007), gr-qc/0610103.
  - [11] B. C. Stephens, M. D. Duez, Y. T. Liu, S. L. Shapiro, and M. Shibata (2007), astro-ph/0702080.
  - [12] E. O'Connor and C. D. Ott, *Astrophys. J.* **730**, 70 (2011), 1010.5550.
  - [13] C. Reisswig, C. Ott, U. Sperhake, and E. Schnetter, *Phys.Rev.* **D83**, 064008 (2011), 1012.0595.
  - [14] B. Giacomazzo, L. Rezzolla, and N. Stergioulas, *Phys.Rev.* **D84**, 024022 (2011), 1105.0122.
  - [15] M. Anderson et al., *Phys. Rev.* **D77**, 024006 (2008), 0708.2720.
  - [16] L. Baiotti, B. Giacomazzo, and L. Rezzolla, *Phys.Rev.* **D78**, 084033 (2008), 0804.0594.
  - [17] Y. T. Liu, S. L. Shapiro, Z. B. Etienne, and K. Taniguchi, *Phys.Rev.* **D78**, 024012 (2008), 0803.4193.
  - [18] M. Anderson et al., *Phys. Rev. Lett.* **100**, 191101 (2008), 0801.4387.
  - [19] K. Hotokezaka, K. Kyutoku, H. Okawa, M. Shibata, and K. Kiuchi, *Phys.Rev.* **D83**, 124008 (2011), 1105.4370.
  - [20] M. Shibata, Y. Suwa, K. Kiuchi, and K. Ioka (2011), \* Temporary entry \*, 1105.3302.
  - [21] M. D. Duez, Y. T. Liu, S. L. Shapiro, M. Shibata, and B. C. Stephens, *Phys. Rev. Lett.* **96**, 031101 (2006), astro-ph/0510653.
  - [22] M. Shibata, M. D. Duez, Y. T. Liu, S. L. Shapiro, and B. C. Stephens, *Phys. Rev. Lett.* **96**, 031102 (2006), astro-ph/0511142.
  - [23] M. D. Duez, Y. T. Liu, S. L. Shapiro, and M. Shibata, *Phys. Rev.* **D73**, 104015 (2006), astro-ph/0605331.
  - [24] K. Kiuchi, M. Shibata, and S. Yoshida, *Phys. Rev.* **D78**, 024029 (2008), 0805.2712.
  - [25] S. L. Liebling, L. Lehner, D. Neilsen, and C. Palenzuela, *Phys. Rev.* **D81**, 124023 (2010), 1001.0575.
  - [26] S. L. Liebling, *Proceedings of the Twelfth Marcel Grossmann Meeting on General Relativity*, Singapore (2011), 1002.2217.
  - [27] B. Giacomazzo, L. Rezzolla, and L. Baiotti, *Mon.Not.Roy.Astron.Soc.* **399**, L164 (2009), 0901.2722.
  - [28] D. J. Price and S. Rosswog, *Science* **312**, 719 (2006), arXiv:astro-ph/0603845.
  - [29] M. Obergaulinger, M. A. Aloy, and E. Müller, *Astronomy and Astrophysics* **515**, A30+ (2010), 1003.6031.
  - [30] T. W. Baumgarte and S. L. Shapiro, *Astrophys. J.* **585**, 930 (2003).
  - [31] P. Goldreich and W. H. Julian, *Astrophys. J.* **157**, 869 (1969).
  - [32] M. Lyutikov, *Phys. Rev.* **D83**, 124035 (2011), 1104.1091.
  - [33] A. Kandus and C. G. Tsagas, *MNRAS* **385**, 883 (2008), 0711.3573.
  - [34] J. D. Bekenstein and E. Oron, *PRD* **18**, 1809 (1978).
  - [35] R. D. Blandford and R. L. Znajek, *Monthly Not. Royal Ast. Soc* **179**, 433 (1977).
  - [36] M. H. Carpenter, D. Gottlieb, and S. Abarbanel, *Applied Numerical Mathematics* **12**, 55 (1993).
  - [37] C. Palenzuela, T. Garrett, L. Lehner, and S. L. Liebling, *Phys. Rev.* **D82**, 044045 (2010), 1007.1198.
  - [38] L. Lehner, O. Reula, and M. Tiglio, *Class. Quant. Grav.* **22**, 5283 (2005), gr-qc/0507004.
  - [39] C. Palenzuela, M. Anderson, L. Lehner, S. L. Liebling, and D. Neilsen, *Phys. Rev. Lett.* **103**, 081101 (2009), 0905.1121.
  - [40] C. Palenzuela, L. Lehner, and S. L. Liebling, *Science* **329**, 927 (2010), 1005.1067.
  - [41] HAD home page (2010), <http://had.liu.edu>.
  - [42] S. L. Liebling, *Phys. Rev. D* **66**, 041703 (2002).
  - [43] L. Lehner, S. L. Liebling, and O. Reula, *Class. Quant. Grav.* **23**, S421 (2006), gr-qc/0510111.
  - [44] F. Pretorius, Ph.D. thesis, The University of British Columbia (2002).
  - [45] M. Anderson, E. Hirschmann, S. L. Liebling, and D. Neilsen, *Class. Quant. Grav.* **23**, 6503 (2006), gr-qc/0605102.
  - [46] LORENE. home page (2010), <http://www.lorene.obspm.fr/>.
  - [47] F. C. Michel, *Astrophys. J.* **180**, 207 (1973).
  - [48] S. S. Komissarov, *MNRAS* **367**, 19 (2006), arXiv:astro-ph/0510310.
  - [49] N. Bucciantini, T. A. Thompson, J. Arons, E. Quataert, and L. Del Zanna, *MNRAS* **368**, 1717 (2006), arXiv:astro-ph/0602475.
  - [50] J. C. McKinney, *MNRAS* **368**, L30 (2006), arXiv:astro-ph/0601411.
  - [51] T. W. Baumgarte and S. L. Shapiro, *Astrophys. J.* **585**, 930 (2003), astro-ph/0211339.
  - [52] C. Thompson and O. Blaes, *Phys.Rev.* **D57**, 3219 (1998).
  - [53] R. C. Duncan, S. L. Shapiro, and I. Wasserman, *Astrophys. J.* **309**, 141 (1986).
  - [54] B. D. Metzger, T. A. Thompson, and E. Quataert, *Astroph. J.* **659**, 561 (2007), arXiv:astro-ph/0608682.
  - [55] E. Berti, V. Cardoso, and A. O. Starinets, *Class.Quant.Grav.* **26**, 163001 (2009), \* Temporary entry \*, 0905.2975.
  - [56] H. Baty, E. R. Priest, and T. G. Forbes, *Physics of Plasmas* **13**, 022312 (2006).
  - [57] M. Lyutikov and J. C. McKinney (2011), \* Temporary entry \*, 1109.0584.
  - [58] M. Lyutikov, *Phys. Rev.* **D83**, 064001 (2011), 1101.0639.
  - [59] B. Paczynski, *Astroph. J.* **494**, L45 (1998), arXiv:astro-ph/9710086.
  - [60] R. C. Duncan and C. Thompson, *Astroph. J.* **392**, L9 (1992).
  - [61] V. V. Usov, *Nature* **357**, 472 (1992).
  - [62] T. A. Thompson, P. Chang, and E. Quataert, *Astroph. J.* **611**, 380 (2004), arXiv:astro-ph/0401555.
  - [63] M. J. Rees and J. E. Gunn, *Mon. Not. R. Astron. Soc.* **167**, 1 (1974).
  - [64] R. D. Blandford and R. L. Znajek, *Mon. Not. R. Astron. Soc.* **179**, 433 (1977).
  - [65] M. A. Ruderman and P. G. Sutherland, *Astroph. J.* **196**, 51 (1975).
  - [66] C. Thompson and O. Blaes, *Phys. Rev. D* **57**, 3219 (1998).
  - [67] A. Spitkovsky, *Astroph. J.* **648**, L51 (2006), arXiv:astro-ph/0603147.
  - [68] R. C. Duncan, S. L. Shapiro, and I. Wasserman, *Astroph. J.* **309**, 141 (1986).
  - [69] L. Dessart, C. D. Ott, A. Burrows, S. Rosswog, and

- E. Livne, *Astroph. J.* **690**, 1681 (2009), 0806.4380.
- [70] C. Kouveliotou, C. A. Meegan, G. J. Fishman, N. P. Bhat, M. S. Briggs, T. M. Koshut, W. S. Paciesas, and G. N. Pendleton, *Astroph. J.* **413**, L101 (1993).
- [71] Y. Sekiguchi, K. Kiuchi, K. Kyutoku, and M. Shibata, *Phys. Rev. Lett.* **107**, 051102 (2011), 1105.2125.
- [72] V. P. Frolov and I. D. Novikov, *Black hole physics : basic concepts and new developments* (Kluwer, 1998).
- [73] S. A. Balbus and J. F. Hawley, *Astroph. J.* **376**, 214 (1991).
- [74] L. Rezzolla et al., *Astrophys. J.* **732**, L6 (2011), 1101.4298.
- [75] M. Obergaulinger, M. A. Aloy, and E. Müller, *Astron. Astrophys.* **515**, A30 (2010), 1003.6031.
- [76] A. I. MacFadyen and S. E. Woosley, *Astroph. J.* **524**, 262 (1999), arXiv:astro-ph/9810274.
- [77] C. Thompson, *Astroph. J.* **651**, 333 (2006), arXiv:astro-ph/0507387.
- [78] D. A. Uzdensky and A. I. MacFadyen, *Astroph. J.* **669**, 546 (2007), arXiv:astro-ph/0609047.
- [79] N. Bucciantini, E. Quataert, B. D. Metzger, T. A. Thompson, J. Arons, and L. Del Zanna, *Mon. Not. R. Astron. Soc.* **396**, 2038 (2009), 0901.3801.
- [80] S. E. Woosley and T. A. Weaver, *Astroph. J. Supp.* **101**, 181 (1995).
- [81] B. D. Metzger, in *New Horizons in Astronomy: Frank N. Bash Symposium 2009*, edited by L. M. Stanford, J. D. Green, L. Hao, & Y. Mao (2010), vol. 432 of *Astronomical Society of the Pacific Conference Series*, p. 81, 1001.5046.
- [82] M. M. Romanova, G. V. Ustyugova, A. V. Koldoba, and R. V. E. Lovelace, *ArXiv e-prints* (2011), 1111.3068.
- [83] C. Thompson and N. Murray, *Astroph. J.* **560**, 339 (2001), arXiv:astro-ph/0105425.
- [84] B. D. Metzger, A. L. Piro, and E. Quataert, *Mon. Not. R. Astron. Soc.* **390**, 781 (2008), 0805.4415.
- [85] C. Thompson, *Astroph. J.* **534**, 915 (2000).
- [86] J. M. Blondin and A. Mezzacappa, *Nature* **445**, 58 (2007), arXiv:astro-ph/0611680.
- [87] W. Iwakami, K. Kotake, N. Ohnishi, S. Yamada, and K. Sawada, *Astroph. J.* **678**, 1207 (2008), 0710.2191.
- [88] R. Fernández, *Astroph. J.* **725**, 1563 (2010), 1003.1730.
- [89] C. Cutler, *Phys. Rev. D* **66**, 084025 (2002), arXiv:gr-qc/0206051.
- [90] C. Thompson and R. C. Duncan, *Mon. Not. R. Astron. Soc.* **275**, 255 (1995).
- [91] H. Baty, E. R. Priest, and T. G. Forbes, *Physics of Plasmas* **13**, 022312 (2006).
- [92] M. A. Shay, J. F. Drake, R. E. Denton, and D. Biskamp, *JGR* **103**, 9165 (1998).
- [93] G. Kowal, A. Lazarian, E. T. Vishniac, and K. Otmianowska-Mazur, *Astrophys. J.* **700**, 63 (2009), 0903.2052.
- [94] E. Nakar and T. Piran, *Nature* **478**, 82 (2011).
- [95] J. Granot, E. Ramirez-Ruiz, G. B. Taylor, D. Eichler, Y. E. Lyubarsky, R. A. M. J. Wijers, B. M. Gaensler, J. D. Gelfand, and C. Kouveliotou, *Astroph. J.* **638**, 391 (2006), arXiv:astro-ph/0503251.
- [96] E. Quataert and A. Gruzinov, *Astroph. J.* **520**, 248 (1999), arXiv:astro-ph/9803112.
- [97] C. Thompson and R. C. Duncan, *Astroph. J.* **473**, 322 (1996).
- [98] K. Hurley, S. E. Boggs, D. M. Smith, R. C. Duncan, R. Lin, A. Zoglauer, S. Krucker and G. Hurford *et al.*, *Nature* **434**, 1098 (2005)
- [99] Y. T. Tanaka, T. Terasawa, N. Kawai, A. Yoshida, I. Yoshikawa, Y. Saito, T. Takashima, and T. Mukai, *Astroph. J.* **665**, L55 (2007), 0706.3123.
- [100] C. Thompson and R. C. Duncan, *Astroph. J.* **473**, 322 (1996).
- [101] G. Cavallo and M. J. Rees, *Mon. Not. R. Astron. Soc.* **183**, 359 (1978).
- [102] A. Shemi and T. Piran, *Astroph. J.* **365**, L55 (1990).
- [103] J. D. Gelfand, Y. E. Lyubarsky, D. Eichler, B. M. Gaensler, G. B. Taylor, J. Granot, K. J. Newton-McGee, E. Ramirez-Ruiz, C. Kouveliotou, and R. A. M. J. Wijers, *Astroph. J.* **634**, L89 (2005), arXiv:astro-ph/0503269.
- [104] G. B. Taylor, J. D. Gelfand, B. M. Gaensler, J. Granot, C. Kouveliotou, R. P. Fender, E. Ramirez-Ruiz, D. Eichler, Y. E. Lyubarsky, M. Garrett, et al., *Astroph. J.* **634**, L93 (2005), arXiv:astro-ph/0504363.
- [105] D. A. Frail, S. R. Kulkarni, and J. S. Bloom, *Nature* **398**, 127 (1999), arXiv:astro-ph/9812457.
- [106] B. D. Metzger and E. Berger (2011), 1108.6056.
- [107] C. Palenzuela, L. Lehner, S. Liebling, D. Neilsen, et al., paper in preparation.
- [108] S. T. McWilliams and J. Levin, *Astrophys. J.* **742**, 90 (2011), 1101.1969.
- [109] S. S. Komissarov, *MNRAS* **382**, 995 (2007), 0708.0323.
- [110] C. Palenzuela, L. Lehner, O. Reula, and L. Rezzolla (2008), 0810.1838.
- [111] M. Takamoto and T. Inoue, *Astrophys. J.* **735**, 113 (2011), 1105.5683.
- [112] B. Zink, E. Schnetter, and M. Tiglio, *Phys. Rev. D* **77**, 103015 (2008), 0712.0353.
- [113] A. L. Piro and C. D. Ott, *Astroph. J.* **736**, 108 (2011), 1104.0252.
- [114] See however the possibility of doing so with recently developed techniques [109–111]
- [115] This could be achieved by using multipatch methods [38, 112] however.
- [116] This is obtained by balancing the spin-up time  $t_{\text{col}}/2$  with the time for an Alfvén wave to propagate from the star out to  $r_{\text{max}}$  along a dipole field line.
- [117] I.e., the one associated with the instantaneous rotation frequency of the star.
- [118] A more stringent condition is that the magnetosphere is able to hold off the accretion flow out to the corotation radius, as was considered recently by [113] in the case of spherical core collapse around a pre-existing, rotating magnetosphere.
- [119] We employ however a different  $\Gamma$  and our implementation does not cope with as large magnetizations as that in [57].